

Abelian and non-Abelian fractionalized states in twisted MoTe₂: A generalized Landau-level theory

Bohao Li,¹ Yunze Ouyang,¹ and Fengcheng Wu^{1, 2, *}

¹*School of Physics and Technology, Wuhan University, Wuhan 430072, China*

²*Wuhan Institute of Quantum Technology, Wuhan 430206, China*

Fractional Chern insulators are lattice analogs of fractional quantum Hall states that realize fractionalized quasiparticles without an external magnetic field. A key strategy to understand and design these phases is to map Chern bands onto Landau levels (LLs). Here, we introduce a universal framework that variationally decomposes Bloch bands into generalized LLs, providing a controlled and quantitative characterization of their effective LL nature. Applying this approach to twisted bilayer MoTe₂ modeled by first-principles-derived moiré Hamiltonians, we find that the first moiré valence band is dominated by the generalized zeroth LL across a broad range of twist angles, facilitating the formation of Abelian fractional Chern insulators in the Jain sequences. The second moiré band, renormalized via Hartree-Fock calculations at hole filling $\nu_h = 2$, is dominated by the generalized first LL at twist angles $\theta = 2.45^\circ$ and 2.13° . At $\theta = 2.45^\circ$, we find numerical evidence for a non-Abelian Moore–Read (MR) state at $\nu_h = 5/2$, with consistent signatures in both the energy spectrum and the particle entanglement spectrum. Interpolation studies further demonstrate an adiabatic connection between this state and the MR state in the conventional first LL. In contrast, at $\theta = 2.13^\circ$, a charge-density-wave state prevails in the competition with the MR state due to the larger bandwidth. Our variational mapping provides a theoretical framework for exploring exotic fractionalized phases, including non-Abelian states, in realistic systems.

I. INTRODUCTION

Fractionalized states are exotic quantum phases in which the elementary excitations are quasiparticles that carry fractional charge and obey anyonic statistics, which can be either Abelian or non-Abelian. A key example is the fractional quantum Hall insulators (FQHIs), which arise in Landau levels (LLs) of a two-dimensional electron system subjected to low temperatures and high perpendicular magnetic fields [1]. The theoretical foundation of these states was first established by Laughlin’s trial many-body wavefunction [2], which describes fractionalized states at simple odd-denominator filling factors, such as the $\nu = 1/3$ state in the zeroth LL, and features quasiparticle excitations that obey Abelian statistics. This framework was later extended to a broader range of odd-denominator filling factors using hierarchy schemes [3, 4] and composite fermion theory [5, 6]. In contrast, even-denominator FQHIs are less common but have been observed at filling factor $\nu = 5/2$ in the first LL [7], where the Moore–Read (MR) state is the leading theoretical candidate [8–10]. The MR state is distinguished by non-Abelian quasiparticle excitations, which have attracted great interest due to their potential for topological quantum computation [11].

The concept of FQHIs has been extended to fractional Chern insulators (FCIs) in lattice model systems, where Chern bands replace the role of LLs [12–16]. Like their continuum counterparts, FCIs exhibit topological ground-state degeneracy on a torus and support fractionalized quasiparticle excitations. Crucially, FCIs can provide a new paradigm for realizing fractionalized phases

without the need for an external magnetic field, emerging instead from spontaneous time-reversal symmetry breaking. The experimental breakthrough in realizing FCIs at zero external magnetic field was marked by the observation of the fractional quantum anomalous Hall effect in twisted bilayer MoTe₂ (tMoTe₂) [17–20] and subsequently in moiré rhombohedral multilayer graphene systems [21, 22]. These experimental observations have not only validated the FCI concept but also spurred a surge of theoretical investigations. These efforts encompass FCIs in the Jain sequence [23–32], fractionalized quasiparticle excitations [33, 34], anomalous composite Fermi liquids [23, 35, 36], as well as proposals for fractional topological insulators [37] and non-Abelian phases [38–44], which elucidates the microscopic mechanisms and emergent properties of these fractionalized phases.

A key theoretical strategy for understanding and designing FCIs is to establish their connections with FQHIs through correspondence between Chern bands and LLs [45–64]. An important result is the identification of Chern bands with ideal quantum geometry that saturates the trace inequality, for which an exact correspondence between the Bloch wave function and the generalized zeroth LL has been established [53]. In this context, the generalized zeroth LL wave function is the conventional zeroth LL modulated by a position-dependent, momentum-independent function $\mathcal{B}(\mathbf{r})$. Such ideal Chern bands can be theoretically realized in twisted bilayer (or multilayer) graphene in the chiral limit [50, 52, 56, 57], as well as in the Aharonov–Casher model under inhomogeneous magnetic field [62, 65].

In realistic materials, Chern bands inevitably deviate from the ideal limit, raising a fundamental question: to what extent, and in what sense, can lattice Chern bands be mapped onto LLs? Addressing this question is cen-

* wufcheng@whu.edu.cn

tral to understanding why certain Chern bands support fractionalized topological phases analogous to those in the fractional quantum Hall effect, while others do not. Moiré materials provide a unique platform for tackling this problem, as their band structures are highly tunable and can approach the ideal Chern-band limit in certain cases. In tMoTe₂, the first moiré valence band closely approximates an ideal Chern band, a property attributed to the layer-pseudospin skyrmion texture [66] that generates an emergent magnetic field within the adiabatic approximation [61, 62]. This band has been mapped to a generalized zeroth LL using a variational approach [63]. Beyond the lowest band, first-principles calculations indicate that the second moiré band at twist angles around $\theta \approx 2^\circ$ exhibits quantum geometric properties resembling those of the first LL [41, 43]. Consistently, exact diagonalization calculations reveal signatures of non-Abelian fractionalized states in this band, analogous to those found in the first LL [39, 41–43]. These results underscore the importance of establishing a quantitative mapping between Chern bands and LLs. Developing a general and systematic framework for such a correspondence is essential for elucidating the conditions under which Chern bands host Abelian and non-Abelian fractionalized phases, and remains a key open problem with implications for moiré systems and topological materials more broadly.

In this work, we develop a variational framework that decomposes realistic Bloch bands into generalized LLs. The generalized LLs with indices greater than zero are extended from the generalized zeroth LL, possessing a quantum geometry that is no longer ideal, while preserving a quantized integrated trace of the quantum metric [67]. Crucially, these generalized LLs form a complete and orthonormal basis, enabling a controlled decomposition of realistic Bloch bands. By introducing a variational mapping approach, we establish a generalized LL representation of the Bloch bands, where the decomposition can be dominated by a specific generalized LL. This dominance is achieved by variationally optimizing the spatially varying function $\mathcal{B}(\mathbf{r})$, thereby maximizing the weight of the targeted generalized LL. This approach provides a concrete route to identifying the effective LL character of moiré Chern bands and to connecting their quantum geometry to the nature of the fractionalized phases they host.

We apply this variational mapping to tMoTe₂ to investigate Abelian and non-Abelian fractionalized states. Our study uses a continuum model for tMoTe₂ in its most generic form, incorporating all symmetry-allowed terms and first-principles derived parameters [68]. In this continuum model, the first moiré band in $+K$ valley have the Chern number $\mathcal{C} = 1$ within the twist angle range of $2.13^\circ \leq \theta \leq 3.89^\circ$ under study. It nearly, though not exactly, saturates the trace inequality. The second moiré band has the same Chern number as that of the first band within a smaller twist angle range $2.13^\circ \leq \theta \leq 2.88^\circ$, and approaches the integrated trace condition of the generalized first LL. We variationally decompose the first (sec-

ond) moiré band into generalized LLs, which reveals that the generalized zeroth (first) LL is the dominant component, establishing a quantitative correspondence between moiré Chern bands and their effective LL counterparts. We emphasize that even if a band's quantum geometry satisfies the integrated trace condition of the generalized first LL, this does not guarantee a corresponding resemblance in their wave functions. Our explicit decomposition is, therefore, crucial to reveal the internal generalized-LL structure of the Bloch bands.

We perform ED studies with Coulomb interactions projected onto both the original wave function and the variationally obtained generalized OLL wave function for the first band. In both cases, the evidence of FCIs is found at hole filling factors $\nu_h = 1/3, 2/5, 3/5$, and $2/3$ in the Jain sequences. At $\nu_h = 2/3$, FCI remains stable within $2.13^\circ \leq \theta \leq 3.89^\circ$. At $\nu_h = 1/3$, FCI remains stable in a narrower region $2.45^\circ \leq \theta \leq 3.48^\circ$, where the system becomes gapless at $\theta = 2.13^\circ$ and transitions into a charge density wave (CDW) state at $\theta = 3.89^\circ$. At $\nu_h = 2/5$ and $3/5$, FCI remains stable within $2.45^\circ \leq \theta \leq 3.89^\circ$ and becomes gapless at $\theta = 2.13^\circ$. The ED spectrum in both models has a good correspondence at the four filling factors, showing that these Abelian fractionalized states in tMoTe₂ are adiabatically connected to their corresponding FQHIs. Furthermore, FCI states are also identified at $\nu_h = 4/7$ within $2.13^\circ \leq \theta \leq 3.89^\circ$, and $\nu_h = 3/7, 5/9$, and $4/9$ within $2.45^\circ \leq \theta \leq 3.89^\circ$, which also belong to the Jain sequences. Numerical evidence for an anomalous composite Fermi liquid is observed at $\nu_h = 1/2$ across the studied range of twist angles.

We investigate the possible non-Abelian state in the second band of tMoTe₂, focusing on the filling factor $\nu_h = 5/2$ and twist angle $\theta = 2.45^\circ$. We first perform a self-consistent Hartree-Fock (HF) calculation at the integer filling $\nu_h = 2$ to construct interaction-renormalized Bloch bands. In this refined basis, we also perform mapping between the second band and the generalized LLs, where the weight of the generalized 1LL is further enhanced compared to the noninteracting case. Experimental results show a ferromagnetic state near $\nu_h = 5/2$ and $\nu_h = 3$ at various twist angles [69–71], indicating a trend of spontaneous valley polarization in the second moiré band. Therefore, we use the renormalized Bloch states to build a projected many-body Hamiltonian at $\nu_h = 5/2$ within the second band and $+K$ valley. We then perform ED calculation, where both the ED spectrum and the particle entanglement spectrum (PES) show consistent evidence of the non-Abelian MR state. Additionally, we perform ED studies using a series of Hamiltonians interpolating between the second band of tMoTe₂ and the first LL. We find a finite gap throughout, indicating that the MR state is adiabatically connected to the corresponding state in the first LL. At a smaller twist angle, $\theta = 2.13^\circ$, although the second band also exhibits a high generalized 1LL weight, ED and PES indicate a charge-density-wave (CDW) state, which is favored over the MR state due to the larger bandwidth.

The rest of this paper is organized as follows. In Section II, we provide a review of generalized LLs and present their quantum geometric properties. Section III is devoted to the continuum model for tMoTe₂, along with a detailed analysis of the first two moiré valence bands across different twist angles. In Section IV, we introduce a variational mapping method to construct a generalized LL representation of Bloch bands, which is then applied to the first two bands of tMoTe₂. Section V investigates Abelian fractional Chern insulators in the first moiré band. Section VI presents the numerical evidence of the MR state in the second moiré band at half filling. Finally, in Section VII we conclude with a summary and a discussion. Additional technical details and numerical results are provided in appendices.

II. GENERALIZED LLs

We begin by reviewing the concept of quantum geometry and introducing the generalized LL wave functions. These generalized LLs extend the standard LL wave function by incorporating spatial modulations and fluctuations in quantum geometry [67]. As a starting point, we present the definition of the quantum geometric tensor (QGT),

$$(\chi_{\mathbf{k}})_{ab} = \langle \partial_{k_a} u_{\mathbf{k}} | (\mathbb{1} - P) | \partial_{k_b} u_{\mathbf{k}} \rangle. \quad (1)$$

Here we focus on the Abelian QGT for a single band of Bloch wave function $\psi_{\mathbf{k}}(\mathbf{r})$ with \mathbf{k} the wave vector. In Eq. (1), $u_{\mathbf{k}}(\mathbf{r}) = e^{-i\mathbf{k} \cdot \mathbf{r}} \psi_{\mathbf{k}}(\mathbf{r})$ is the periodic part of $\psi_{\mathbf{k}}(\mathbf{r})$, $P = |u_{\mathbf{k}}\rangle \langle u_{\mathbf{k}}|$ is the projection operator, and a, b denote spatial indices. We focus on two dimensions here. The Berry curvature $\Omega_{\mathbf{k}}$ and quantum metric $g_{\mathbf{k}}$ are derived from Eq. (1) through the relation $(\chi_{\mathbf{k}})_{ab} = (g_{\mathbf{k}})_{ab} - \frac{i}{2} \epsilon_{ab} \Omega_{\mathbf{k}}$, where ϵ_{ab} is the Levi-Civita symbol. Here $\chi_{\mathbf{k}}$ is a Hermitian matrix, $g_{\mathbf{k}}$ is a real symmetric matrix, and $\Omega_{\mathbf{k}}$ is a real function. Because $\mathbb{1} - P$ is a projector, the QGT is semipositive definite, which implies that $\det[g_{\mathbf{k}}] \geq \Omega_{\mathbf{k}}^2/4$. Since $g_{\mathbf{k}}$ is a 2×2 real symmetric matrix, $(\text{Tr}[g_{\mathbf{k}}])^2 \geq 4 \det[g_{\mathbf{k}}]$. Therefore, there is a trace inequality $\text{Tr}[g_{\mathbf{k}}] \geq |\Omega_{\mathbf{k}}|$.

The integrals of the Berry curvature and the trace of quantum metric over the Brillouin zone give rise to, respectively, the Chern number \mathcal{C} and the quantum weight \mathcal{K} [72],

$$\begin{aligned} \mathcal{C} &= \frac{1}{2\pi} \int d\mathbf{k} \Omega_{\mathbf{k}}, \\ \mathcal{K} &= \frac{1}{2\pi} \int d\mathbf{k} \text{Tr}[g_{\mathbf{k}}]. \end{aligned} \quad (2)$$

Here, \mathcal{C} is a topological invariant that is quantized to an integer value, whereas \mathcal{K} is not. Because of the inequality $\text{Tr}[g_{\mathbf{k}}] \geq |\Omega_{\mathbf{k}}|$, we have $\mathcal{K} \geq |\mathcal{C}|$, which represents an alternative form of the trace inequality. As discussed below, both \mathcal{C} and \mathcal{K} provide important insights into the

quantum geometry, complementing the information captured by the QGT.

A prototypical example of topological bands with finite Chern numbers is the LLs formed in two-dimensional electron gas subjected to a perpendicular magnetic field. The wave function of LLs satisfying magnetic translational symmetry is the magnetic Bloch wave function given by $\Psi_{n,\mathbf{k}}^{(s)}(\mathbf{r})$ [73], where $n \geq 0$ is the LL index, \mathbf{k} is the magnetic translation quantum number and $s = \pm$ denote the orientation of magnetic field. We present the form of $\Psi_{n,\mathbf{k}}^{(s)}(\mathbf{r})$ in Appendix A. The QGT for the n th LL (n LL), with wave function $\Psi_{n,\mathbf{k}}^{(s)}(\mathbf{r})$, is

$$\chi_{\mathbf{k},n,s}^{(\text{LL})} = \begin{pmatrix} n + \frac{1}{2} & -\frac{is}{2} \\ \frac{is}{2} & n + \frac{1}{2} \end{pmatrix} \ell^2, \quad (3)$$

where ℓ is the magnetic length. The magnetic unit cell, which contains one flux quantum, has an area of $2\pi\ell^2$. The QGT for the n LL is momentum-independent, characterized by $\text{Tr}[g_{\mathbf{k}}] = (2n + 1)\ell^2$ and $|\Omega_{\mathbf{k}}| = \ell^2$. These satisfy the relation $\text{Tr}[g_{\mathbf{k}}] = (2n + 1)|\Omega_{\mathbf{k}}|$ at each momentum \mathbf{k} . The 0LL is special in that it saturates the trace inequality $\text{Tr}[g_{\mathbf{k}}] \geq |\Omega_{\mathbf{k}}|$. Because $|\Omega_{\mathbf{k}}| = \ell^2$ is independent of the LL index n , each LL has a Chern number with a magnitude $|\mathcal{C}| = 1$. However, the quantum weight \mathcal{K} depends on the LL index n , given by $\mathcal{K} = 2n + 1$.

The property of the 0LL motivates the construction of more general Bloch states that also saturate the trace inequality, which are generalized 0LL with wave function given by

$$\Theta_{0,\mathbf{k}}^{(s)}(\mathbf{r}) = \mathcal{N}_{0,\mathbf{k}} \mathcal{B}^{(s)}(\mathbf{r}) \Psi_{0,\mathbf{k}}^{(s)}(\mathbf{r}). \quad (4)$$

Here $\mathcal{B}^{(s)}(\mathbf{r})$ is a position \mathbf{r} -dependent but momentum \mathbf{k} -independent function, and $\mathcal{N}_{0,\mathbf{k}}$ is a normalization factor. Due to the spatial modulation introduced by $\mathcal{B}^{(s)}(\mathbf{r})$, the QGT of $\Theta_{0,\mathbf{k}}^{(s)}(\mathbf{r})$ acquires momentum dependence. Nevertheless, it still satisfies the equality $\text{Tr}[g_{\mathbf{k}}] = |\Omega_{\mathbf{k}}|$ at each momentum \mathbf{k} , a condition known as ideal quantum geometry [53]. The Chern number and quantum weight associated with $\Theta_{0,\mathbf{k}}^{(s)}(\mathbf{r})$ remain the same as those of the 0LL, given by $\mathcal{K} = |\mathcal{C}| = 1$. An important feature of the generalized 0LL described by $\Theta_{0,\mathbf{k}}^{(s)}(\mathbf{r})$ is that it enables construction of trial wave functions for fractional Chern insulators (FCIs) [51, 53]. The trial state takes the form $\Phi_F = \Psi_F \prod_i \mathcal{B}^{(s)}(\mathbf{r}_i)$, where \mathbf{r}_i denotes the position of the i th electron, and Ψ_F is a fractional quantum Hall state in the 0LL. In certain cases, Φ_F can serve as the exact ground state of short-range repulsive interactions at special filling factors [53].

Recent theoretical developments show that the generalized n LL wave function $\Theta_{n,\mathbf{k}}^{(s)}(\mathbf{r})$ for $n \geq 1$ can be systematically constructed by applying Gram–Schmidt orthogonalization to a set of density-modulated basis functions $e_{n,\mathbf{k}}^{(s)}(\mathbf{r})$ [67], defined as,

$$e_{n,\mathbf{k}}^{(s)}(\mathbf{r}) = \mathcal{B}^{(s)}(\mathbf{r}) \Psi_{n,\mathbf{k}}^{(s)}(\mathbf{r}). \quad (5)$$

Here $\mathcal{B}^{(s)}(\mathbf{r})$ introduces spatial modulation and $\Psi_{n,\mathbf{k}}^{(s)}(\mathbf{r})$ is the magnetic Bloch wave function of the conventional n LL. The generalized LL wave function $\Theta_{n,\mathbf{k}}^{(s)}(\mathbf{r})$ is then given by,

$$\Theta_{n,\mathbf{k}}^{(s)}(\mathbf{r}) = \begin{cases} \mathcal{N}_{0,\mathbf{k}} e_{0,\mathbf{k}}^{(s)}(\mathbf{r}) & n = 0 \\ \mathcal{N}_{n,\mathbf{k}} [e_{n,\mathbf{k}}^{(s)}(\mathbf{r}) - \sum_{m=0}^{n-1} \langle \Theta_{m,\mathbf{k}}^{(s)} | e_{n,\mathbf{k}}^{(s)} \rangle \Theta_{m,\mathbf{k}}^{(s)}(\mathbf{r})] & n \geq 1, \end{cases} \quad (6)$$

where $\mathcal{N}_{n,\mathbf{k}}$ is the normalization factor. For $n \geq 1$, the QGT of $\Theta_{n,\mathbf{k}}^{(s)}(\mathbf{r})$ is generally momentum dependent and does *not* obey the local trace condition of $\text{Tr}[g_{\mathbf{k}}] = (2n+1)|\Omega_{\mathbf{k}}|$, but follows the integrated form of the trace condition (see Ref. [67] and also Appendix B for proof),

$$\mathcal{K} = (2n+1)|\mathcal{C}| = 2n+1. \quad (7)$$

We emphasize that while a band with $\mathcal{K} = |\mathcal{C}| = 1$ admits a universal wave function—the generalized 0LL given in Eq. (4)—this universality breaks down for higher indices. Specifically, for $n > 0$, even if a band satisfies Eq. (7), it does not necessarily realize the generalized n LL as its wave function.

The generalized n LL wave functions $\Theta_{n,\mathbf{k}}^{(s)}(\mathbf{r})$ can form a complete and orthonormal basis for decomposing Bloch bands. In this work, we focus on Chern bands in tMoTe₂, where the wave functions are expressed in the layer pseudospin-1/2 space. Therefore, we consider a two-component $\mathcal{B}^{(s)}(\mathbf{r})$ to account for the layer degree of freedom. Moreover, we require that the two-component spinors $\mathcal{B}^{(+)}(\mathbf{r})$ and $\mathcal{B}^{(-)}(\mathbf{r})$ are orthogonal at each position \mathbf{r} , which ensures the following orthonormal condition,

$$\langle \Theta_{n,\mathbf{k}}^{(s)} | \Theta_{n',\mathbf{k}}^{(s')} \rangle = \delta_{n,n'} \delta_{s,s'}. \quad (8)$$

In our work, we further require that $\Theta_{n,\mathbf{k}}^{(s)}(\mathbf{r})$ obeys Bloch theorem instead of magnetic Bloch theorem, which puts constraints on the translational symmetry of $\mathcal{B}^{(s)}(\mathbf{r})$ (see Appendix A for discussion).

III. MOIRÉ BANDS

In tMoTe₂, the single-particle moiré Hamiltonian for valence-band states can be constructed independently for the $+K$ and $-K$ valleys. We focus on the $+K$ valley, as the $-K$ -valley Hamiltonian follows from it via time-reversal symmetry \mathcal{T} . The continuum moiré Hamiltonian is typically represented as a 2×2 matrix in the layer-pseudospin basis, incorporating quadratic kinetic terms as well as the lowest-harmonic intralayer potentials and interlayer tunneling terms [66]. In this work, we adopt the moiré Hamiltonian in the most generic form following Ref. [68], which includes (i) generalized kinetic-energy terms beyond the quadratic approximation and (ii) a momentum-dependent potential terms beyond the

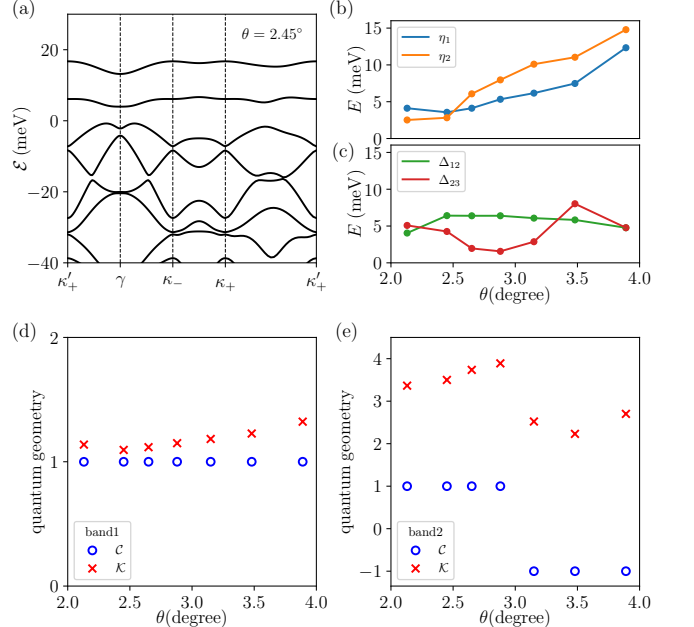


FIG. 1. (a) Moiré band structure of tMoTe₂ in $+K$ valley at $\theta = 2.45^\circ$ along high-symmetry path in the mBZ. (b) Bandwidths of the first moiré band η_1 and the second moiré band η_2 as functions of θ . (c) Energy gaps Δ_{12} between the first and second bands, and Δ_{23} between the second and third bands, plotted as a function of θ . (d) Chern number \mathcal{C} and quantum weight \mathcal{K} for the first moiré valence band in $+K$ valley. (e) Same as (d), but for the second moiré band. Results are shown for commensurate angles θ at $2.13^\circ, 2.45^\circ, 2.65^\circ, 2.88^\circ, 3.15^\circ, 3.48^\circ$ and 3.89° .

lowest-harmonic approximation. The $+K$ -valley Hamiltonian is then given by

$$H_+ = U_0(\mathbf{r}) \begin{pmatrix} H_b^0(\hat{\mathbf{k}}) + \Delta_b(\hat{\mathbf{k}}, \mathbf{r}) & \Delta_T(\hat{\mathbf{k}}, \mathbf{r}) \\ \Delta_T^\dagger(\hat{\mathbf{k}}, \mathbf{r}) & H_t^0(\hat{\mathbf{k}}) + \Delta_t(\hat{\mathbf{k}}, \mathbf{r}) \end{pmatrix} U_0^\dagger(\mathbf{r}), \quad (9)$$

where $H_l^0(\hat{\mathbf{k}})$ denotes the layer-dependent kinetic term, $\Delta_l(\hat{\mathbf{k}}, \mathbf{r})$ is the momentum-dependent intralayer moiré potential, $\Delta_T(\hat{\mathbf{k}}, \mathbf{r})$ the momentum-dependent interlayer tunneling term, and $l = b, t$ labels the layers. The unitary matrix $U_0(\mathbf{r}) = \text{diag}(e^{i\kappa_+ \cdot \mathbf{r}}, e^{i\kappa_- \cdot \mathbf{r}})$ is employed to render the Hamiltonian in a more symmetric and compact form, where $\kappa_\pm = \frac{4\pi}{3a_M}(-\frac{\sqrt{3}}{2}, \mp\frac{1}{2})$ are located at corners of moiré Brillouin zone (mBZ), $a_M \approx a_0/\theta$ is the moiré period, θ is the twist angle, and $a_0 = 3.52$ Å is the monolayer lattice constant. $H_l^0(\hat{\mathbf{k}})$, $\Delta_l(\hat{\mathbf{k}}, \mathbf{r})$, and $\Delta_T(\hat{\mathbf{k}}, \mathbf{r})$ can be expressed as a series expansion in the momentum operator $\hat{\mathbf{k}}$ and a harmonic expansion in the position operator \mathbf{r} .

The kinetic energy $H_l^0(\hat{\mathbf{k}})$ is parametrized as,

$$H_l^0(\hat{\mathbf{k}}) = \sum_{M_1, M_2} \frac{\hbar^2}{2m_l^{(M_1, M_2)}} f_{\hat{\mathbf{k}}}^{(M_1, M_2)}, \quad (10)$$

where $f_{\hat{\mathbf{k}}}^{(M_1, M_2)} = (\hat{k}_x + i\hat{k}_y)^{M_1}(\hat{k}_x - i\hat{k}_y)^{M_2}$ forms a polynomial basis in $\hat{\mathbf{k}}$, $M_{1,2} \in \mathbb{N}_0$ and $\hbar^2/(2m_l^{(M_1, M_2)})$ is the corresponding expansion coefficient. Equation (10) reduces to the conventional parabolic kinetic term when $m_l^{(M_1, M_2)}$ is infinite for all $(M_1, M_2) \neq (1, 1)$.

The intralayer potential $\Delta_l(\hat{\mathbf{k}}, \mathbf{r})$ takes the form

$$\Delta_l(\hat{\mathbf{k}}, \mathbf{r}) = \sum_{M_1, M_2, \mathbf{g}} V_{\mathbf{g}, l}^{(M_1, M_2)} f_{\hat{\mathbf{k}}}^{(M_1, M_2)} e^{i\mathbf{g} \cdot \mathbf{r}} + \text{h.c.}, \quad (11)$$

where $V_{\mathbf{g}, l}^{(M_1, M_2)}$ is the expansion coefficient, \mathbf{g} is the moiré reciprocal lattice vector defined as $\mathbf{g} = m\mathbf{g}_1 + n\mathbf{g}_2$ with $m, n \in \mathbb{Z}$ and $\mathbf{g}_j = \frac{4\pi}{\sqrt{3}a_M} [\cos \frac{(j-1)\pi}{3}, \sin \frac{(j-1)\pi}{3}]$.

The interlayer tunneling term $\Delta_T(\hat{\mathbf{k}}, \mathbf{r})$ is given by

$$\Delta_T(\hat{\mathbf{k}}, \mathbf{r}) = \sum_{M_1, M_2, \mathbf{q}} w_{\mathbf{q}}^{(M_1, M_2)} [f_{\hat{\mathbf{k}}}^{(M_1, M_2)} e^{-i\mathbf{q} \cdot \mathbf{r}} + e^{i(\hat{R}_{2x}\mathbf{q}) \cdot \mathbf{r}} f_{\hat{\mathbf{k}}}^{(M_2, M_1)}], \quad (12)$$

where $w_{\mathbf{q}}^{(M_1, M_2)}$ is the expansion coefficient, \hat{R}_{2x} is the two-fold rotational operator around x -axis, $\mathbf{q} = \mathbf{g} + \mathbf{q}_1$ and $\mathbf{q}_1 = \boldsymbol{\kappa}_+ - \boldsymbol{\kappa}_-$. $\Delta_l(\hat{\mathbf{k}}, \mathbf{r})$ and $\Delta_T(\hat{\mathbf{k}}, \mathbf{r})$ become momentum-independent when $V_{\mathbf{g}, l}^{(M_1, M_2)} = 0$ and $w_{\mathbf{q}}^{(M_1, M_2)} = 0$ for $(M_1, M_2) \neq (0, 0)$.

The point group symmetry of tMoTe₂ is D_3 , which includes the C_{3z} and C_{2y} symmetries. Here, C_{nj} represents an n -fold rotation about the j -axis. The valley-projected Hamiltonian in Eq. (9) is required to be Hermitian and to remain invariant under the C_{3z} and $C_{2y}\mathcal{T}$ symmetries. As a consequence, the parameters in Eqs. (10), (11), and (12) are constrained by the following conditions

$$\begin{aligned} m_l^{(M_1, M_2)} &= [m_l^{(M_2, M_1)}]^* = [m_{-l}^{(M_1, M_2)}]^*, \\ V_{\mathbf{g}, l}^{(M_1, M_2)} &= \omega^{M_1 - M_2} V_{\hat{R}_3 \mathbf{g}, l}^{(M_1, M_2)}, V_{\mathbf{g}, l}^{(M_1, M_2)} = [V_{\hat{R}_{2x} \mathbf{g}, -l}^{(M_1, M_2)}]^*, \\ w_{\mathbf{q}}^{(M_1, M_2)} &= \omega^{M_1 - M_2} w_{\hat{R}_3 \mathbf{q}}^{(M_1, M_2)}, \end{aligned} \quad (13)$$

where $\omega = e^{i2\pi/3}$ and $m_l^{(M_1, M_2)}$ is finite only if $M_1 - M_2 \equiv 0 \pmod{3}$.

A first-principles-based framework for constructing the general moiré Hamiltonian, free of any empirical fitting, was developed in Ref. [68]. Using this approach, the θ -dependent model parameters for several commensurate twist angles within the range $\theta \in [2.13^\circ, 3.89^\circ]$ were obtained. In the present work, we adopt the parameters from the full continuum model constructed in Ref. [68] (the corresponding parameters are extracted from Ref. [74]), which achieves energy deviations below 0.5 meV and wavefunction overlaps exceeding 97% for the four highest-energy bands, compared to the first-principles results in the standard basis of pseudo-atomic orbital functions.

A representative moiré band structure in $+K$ valley at $\theta = 2.45^\circ$ is shown in Fig. 1(a). The top two moiré bands are energetically isolated and exhibit a narrow

bandwidth. Figure 1(b) shows the bandwidth η_1 and η_2 of the first (i.e., topmost) and second moiré bands, respectively. Both η_1 and η_2 are relatively small, below 5 meV for $\theta \leq 2.45^\circ$, and stay under 15 meV for θ up to 3.89° , indicating the bands retain a notably flat character over this range. We further plot the band gap $\Delta_{n(n+1)}$ between the n th and $(n+1)$ th moiré valence bands in Fig. 1(c). For the plotted range of θ , Δ_{12} remains finite, on the order of 5 meV. However, Δ_{23} has a minimum near $\theta = 3^\circ$, implying a topological phase transition in the second moiré band as explained below.

To characterize the quantum geometry of the first two bands, we plot the Chern number \mathcal{C} and quantum weight \mathcal{K} as functions of θ in Figs. 1(d) and 1(e). For the first moiré valence band, \mathcal{C} is quantized to +1 within $\theta \in [2.13^\circ, 3.89^\circ]$, and \mathcal{K} exceeds $|\mathcal{C}|$ as expected, with only a small difference between them. The $\mathcal{K} - |\mathcal{C}|$ value, which quantifies the deviation from ideal quantum geometry, remains below 0.5 across the entire θ range and reaches a minimum of 0.095 at $\theta = 2.45^\circ$, suggesting a strong connection between the first moiré valence band and the generalized 0LL.

In contrast, the second moiré valence band exhibits a Chern number $\mathcal{C} = +1$ at small twist angles but undergoes a sign reversal to -1 above a critical angle θ_c between 2.88° and 3.15° . For $\theta < \theta_c$, \mathcal{K} is close to $3|\mathcal{C}|$. Motivated by Eq. (7), the quantity $\mathcal{K} - 3|\mathcal{C}|$ serves as a measure of similarity between the second moiré band and the generalized 1LL. This difference decreases with decreasing θ below θ_c and reaches a minimum of 0.37 at $\theta = 2.13^\circ$, indicating a potential correspondence between the second moiré band and the generalized 1LL.

IV. VARIATIONAL MAPPING

We now introduce a variational mapping approach to establish a generalized LL representation of Bloch bands, and apply it to the first two moiré bands in the tMoTe₂ model. The Bloch wave function $\psi_{+,m,\mathbf{k}}(\mathbf{r})$ of the m th band at momentum \mathbf{k} and $+K$ valley can be decomposed in terms of the generalized LL wave functions $\Theta_{n,\mathbf{k}}^{(s)}(\mathbf{r})$,

$$\psi_{+,m,\mathbf{k}}(\mathbf{r}) = \sum_n \sum_{s=\pm} c_{m,n,\mathbf{k}}^{(s)} \Theta_{n,\mathbf{k}}^{(s)}(\mathbf{r}), \quad (14)$$

where $c_{m,n,\mathbf{k}}^{(s)}$ are the expansion coefficient. This decomposition is general as long as $\psi_{+,m,\mathbf{k}}(\mathbf{r})$ and $\Theta_{n,\mathbf{k}}^{(s)}(\mathbf{r})$ share the same translational symmetry, in accordance with Bloch's theorem. To ensure this, we require that the magnetic Bloch wave function $\Psi_{n,\mathbf{k}}^{(s)}(\mathbf{r})$, used in the definition of $\Theta_{n,\mathbf{k}}^{(s)}(\mathbf{r})$, is defined with respect to a magnetic unit cell that matches exactly with the moiré unit cell of tMoTe₂. This give the relation between the magnetic length ℓ and the moiré period a_M , $2\pi\ell^2 = \sqrt{3}a_M^2/2$.

Using the orthonormality condition in Eq. (8), $c_{m,n,\mathbf{k}}^{(s)}$ can be expressed as the overlap between $\psi_{+,m,\mathbf{k}}(\mathbf{r})$ and

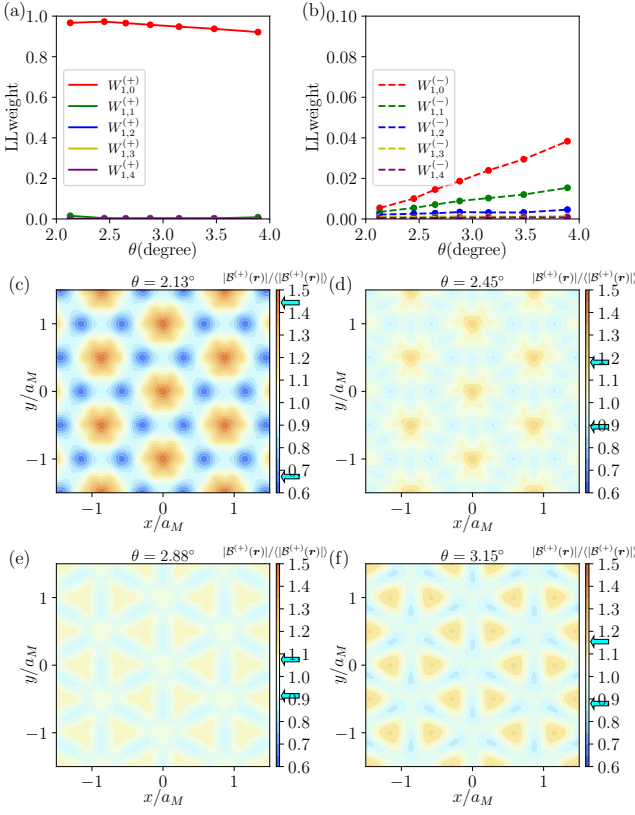


FIG. 2. (a-b) LL weight $W_{m,n}^{(s)}$ for the first moiré band where n and $s = \pm$ label, respectively, the index and chirality of the generalized LL. (c-f) Map of $|\mathcal{B}^{(+)}(\mathbf{r})|$ scaled by its spatial average at $\theta = 2.13^\circ, 2.45^\circ, 2.88^\circ$, and 3.15° . The arrows indicate the data range in each plot.

$\Theta_{n,\mathbf{k}}^{(s)}(\mathbf{r})$, $c_{m,n,\mathbf{k}}^{(s)} = \langle \Theta_{n,\mathbf{k}}^{(s)} | \psi_{+,m,\mathbf{k}} \rangle$. To measure the average overlap between $\psi_{+,m,\mathbf{k}}(\mathbf{r})$ and $\Theta_{n,\mathbf{k}}^{(s)}(\mathbf{r})$, we define the generalized LL weight,

$$W_{m,n}^{(s)} = \frac{1}{N} \sum_{\mathbf{k}} |c_{m,n,\mathbf{k}}^{(s)}|^2, \quad (15)$$

where N is the number of \mathbf{k} points summed within the mBZ.

The spatially varying functions $\mathcal{B}^{(s)}(\mathbf{r})$ are so far arbitrary, provided they respect the necessary translational symmetry to ensure that $\Theta_{n,\mathbf{k}}^{(s)}(\mathbf{r})$ is a Bloch wave function. However, for the decomposition in Eq. (14) to yield physical insight, we would require that a specific generalized LL, $\Theta_{n_0,\mathbf{k}}^{(s_0)}(\mathbf{r})$, contributes a dominant weight $W_{m,n_0}^{(s_0)}$, compared to all other $W_{m,n}^{(s)}$. This can ensure that the dominant contribution to the wave function comes from a well-defined set of states, simplifying the physical interpretation and enabling insights from LL physics. The choice of n_0 and s_0 can be motivated by the quantum geometric properties of the targeted Bloch wave function $\psi_{+,m,\mathbf{k}}(\mathbf{r})$, as explained below. We can then maximize $W_{m,n_0}^{(s_0)}$ variationally by adjusting $\mathcal{B}^{(s_0)}(\mathbf{r})$ via gradient

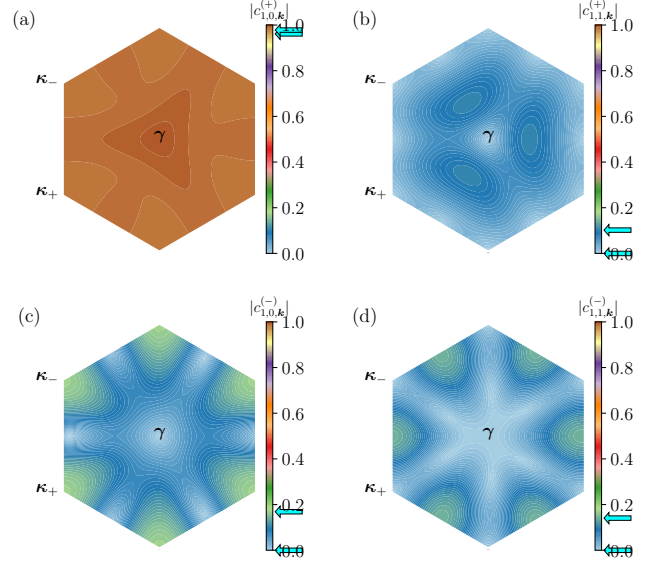


FIG. 3. (a-d) Overlap $|c_{1,n,\mathbf{k}}^{(s)}| = |\langle \Theta_{n,\mathbf{k}}^{(s)} | \psi_{+,1,\mathbf{k}} \rangle|$ at $\theta = 2.45^\circ$ for $s = \pm$ and $n = 0, 1$ in the mBZ. The arrows indicate the data range in each plot.

ascent, starting from an initial ansatz and iterating until convergence:

$$\mathcal{B}_i^{(s_0)}(\mathbf{r}) \rightarrow \mathcal{B}_i^{(s_0)}(\mathbf{r}) + \zeta \frac{\delta W_{m,n_0}^{(s_0)}}{\delta \mathcal{B}_i^{(s_0)}(\mathbf{r})}, \quad (16)$$

where the subscript $i = 1, 2$ labels the i th component of the spinor $\mathcal{B}^{(s_0)}(\mathbf{r})$, and ζ is a positive parameter. Here the functional derivative is defined as

$$\frac{\delta f}{\delta \overline{g}} = \frac{1}{2} \left[\frac{\delta f}{\delta \text{Re}[g]} + i \frac{\delta f}{\delta \text{Im}[g]} \right], \quad (17)$$

for a real function f .

We can further determine $\mathcal{B}^{(-s_0)}(\mathbf{r})$ by noting it is a two-component spinor orthogonal to $\mathcal{B}^{(s_0)}(\mathbf{r})$ at every \mathbf{r} . With this set of procedures, we can calculate all the coefficients $c_{m,n,\mathbf{k}}^{(s)}$ and the weights $W_{m,n}^{(s)}$.

A. The first moiré band

We first apply the variational mapping approach to the first moiré valence band in tMoTe₂. Based on its OLL-like feature of quantum geometry with $\mathcal{C} = +1$ and $\mathcal{K} - |\mathcal{C}| \ll 1$, the dominant generalized LL weight is expected to be $W_{1,0}^{(+)}$. For our initial ansatz of $\mathcal{B}^{(+)}(\mathbf{r})$, we take a simple ratio between the Bloch wave function $\psi_{+,1,\gamma}(\mathbf{r})$ of the first moiré valence band at the γ point and the corresponding OLL wave function $\Psi_{0,\gamma}^{(+)}(\mathbf{r})$,

$$\mathcal{B}^{(+)}(\mathbf{r}) \rightarrow \frac{\psi_{+,1,\gamma}(\mathbf{r})}{\Psi_{0,\gamma}^{(+)}(\mathbf{r})}, \quad (18)$$

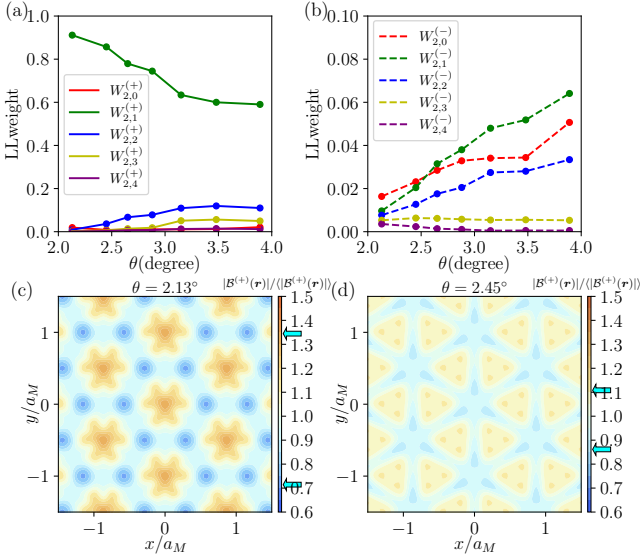


FIG. 4. (a-b) LL weight $W_{2,n}^{(s)}$ for the second moiré band where n and $s = \pm$ label, respectively, the index and chirality of the generalized LL. (c-d) Map of $|\mathcal{B}(\mathbf{r})|$ scaled by its spatial average at $\theta = 2.13^\circ$ and 2.45° . The arrows indicate the data range in each plot.

In this construction, any zeros in the numerator and denominator cancel, ensuring that this initial ansatz is continuous across the entire real space. After adjusting $\mathcal{B}^{(+)}(\mathbf{r})$ according to Eq. (16) until convergence, its orthogonal counterpart $\mathcal{B}^{(-)}(\mathbf{r})$ is obtained via

$$U_0^\dagger(\mathbf{r})\mathcal{B}^{(-)}(\mathbf{r}) = i\sigma_y[U_0^\dagger(\mathbf{r})\mathcal{B}^{(+)}(\mathbf{r})]^*, \quad (19)$$

where σ_y is the y Pauli matrix in the layer pseudospin space. In addition to the orthogonality, this construction ensures that $\Theta_{n,\mathbf{k}}^{(-)}(\mathbf{r})$ satisfies C_{3z} symmetry at three high-symmetry points $\mathbf{k} \in \{\kappa_\pm, \gamma\}$, and respects $C_{2y}\mathcal{T}$ symmetry at γ , as demonstrated in Appendix A.

The resulting generalized LL weights are shown in Figs. 2(a) and 2(b). Throughout the entire θ range, $W_{1,0}^{(+)}$ is the dominant weight as anticipated and exceeds 0.9, while all other weights are smaller by at least an order of magnitude. The cumulative weight for $n \leq 4$, $\sum_{s=\pm} \sum_{n=0}^4 W_{1,n}^{(s)}$, exceeds 0.99 for all twist angles studied. $W_{1,0}^{(+)}$ attains its maximum value of 0.97 at $\theta = 2.45^\circ$, where $\mathcal{K} - |\mathcal{C}|$ is minimized. In Figs. 2(c-f) we present the map of $|\mathcal{B}^{(+)}(\mathbf{r})|$ in real space at four representative twist angles $\theta = 2.13^\circ, 2.45^\circ, 2.88^\circ$, and 3.15° . Here $|\mathcal{B}^{(+)}(\mathbf{r})|$ exhibits spatial modulations following the electron density variation of the first moiré band. At $\theta = 2.13^\circ$, $|\mathcal{B}^{(+)}(\mathbf{r})|$ displays relatively strong spatial fluctuation, with its maximal positions forming an effective triangular lattice. As θ increases, the arrangement of maxima in $|\mathcal{B}^{(+)}(\mathbf{r})|$ gradually evolves from the triangular to its dual honeycomb geometry. Meanwhile, the spatial fluctuations in $|\mathcal{B}^{(+)}(\mathbf{r})|$ weaken as θ increases from 2.13° to

2.88° , but re-intensifies at larger θ .

Figure 3 shows $|c_{1,n,\mathbf{k}}^{(s)}|$ in momentum space for $s = \pm$ and $n = 0, 1$ at $\theta = 2.45^\circ$. Each amplitude $|c_{1,n,\mathbf{k}}^{(s)}|$ exhibits threefold rotational symmetry in the mBZ and is invariant under $k_y \rightarrow -k_y$, as a consequence of the C_{3z} and $C_{2y}\mathcal{T}$ symmetries. Notably, the dominant coefficient $|c_{1,0,\mathbf{k}}^{(+)}|$ is above 0.98 throughout the mBZ, and it maximizes at the γ point, reaching nearly 1.0, thereby confirming the validity of the ansatz in Eq. (18). An adiabatic connection between the moiré band wave function $\psi_{+,1,\mathbf{k}}(\mathbf{r})$ and the generalized 0LL can be established by gradually tuning $c_{1,n,\mathbf{k}}^{(s)}$ to the configuration where $c_{1,0,\mathbf{k}}^{(+)} = 1$ and all other coefficients vanish. We further note that $c_{1,1,\mathbf{k}}^{(+)}$ vanishes at the C_{3z} invariant momenta γ , κ_+ , and κ_- , because the wave functions $\psi_{+,1,\mathbf{k}}(\mathbf{r})$ and $\Theta_{1,\mathbf{k}}^{(+)}$ carry different angular momenta under C_{3z} at these momenta and are therefore orthogonal. The same reasoning explains the zeros of $c_{1,0,\mathbf{k}}^{(-)}$ at γ and of $c_{1,1,\mathbf{k}}^{(-)}$ at γ and κ_\pm .

B. The second moiré band

We turn to the second moiré valence band of $t\text{MoTe}_2$. Near $\theta = 2.13^\circ$, this band exhibits quantum-geometric features analogous to the generalized 1LL, characterized by $\mathcal{C} = +1$ and $\mathcal{K} = 3\mathcal{C}$. Since \mathcal{K} is close to $3\mathcal{C}$, we choose the dominant generalized LL weight to be $W_{2,1}^{(+)}$. The Chern number of this band changes sign for $\theta \geq 3.15^\circ$ due to band inversion with the third band at the γ point. Since the associated wave-function changes are mainly for momenta around γ , $W_{2,1}^{(+)}$ should remain as the leading weight. We therefore maximize $W_{2,1}^{(+)}$ across the full range of θ considered. For the initial ansatz, we use $\mathcal{B}^{(+)}(\mathbf{r})$ obtained from optimizing $W_{1,0}^{(+)}$, and refine it to enhance $W_{2,1}^{(+)}$ within the variational scheme described above. Finally, $\mathcal{B}^{(-)}(\mathbf{r})$ is obtained again from Eq. (19).

Figures 4(a) and 4(b) present the resulting generalized LL weights for the second moiré valence band. In this case, $W_{2,1}^{(+)}$ indeed dominates for $\theta \in [2.13^\circ, 3.89^\circ]$, reaching a maximum of 0.91 at $\theta = 2.13^\circ$ and decreasing to 0.6 at $\theta = 3.89^\circ$. The second-largest weight $W_{2,2}^{(+)}$ rises to 0.1 at $\theta = 3.89^\circ$, while all $W_{2,n}^{(-)}$ remain below 0.1. Importantly, the emergence of a dominant generalized 1LL component is nontrivial: although the quantum weight \mathcal{K} of the second band lies close to $3|\mathcal{C}|$, this condition alone does not a priori ensure a generalized 1LL-like wave function. Therefore, the explicit decomposition into generalized LLs is essential for unambiguously establishing the 1LL-like nature of the second moiré band.

The spatial profiles of the resulting $|\mathcal{B}^{(+)}(\mathbf{r})|$ are shown in Figs. 4(c) and 4(d) for $\theta = 2.13^\circ$ and $\theta = 2.45^\circ$, respectively, where the arrangement of maxima evolves from a triangular to its dual honeycomb geometry, similar to the

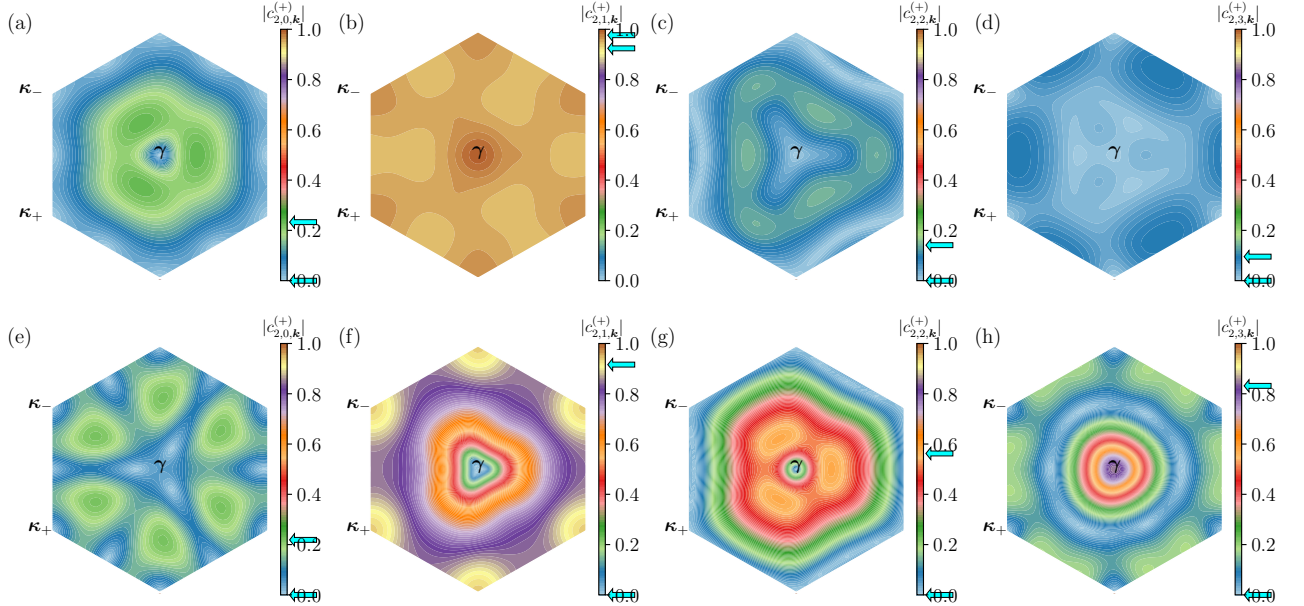


FIG. 5. Overlap $|c_{2,n,k}^{(+)}| = |\langle \Theta_{n,k}^{(+)} | \psi_{+,2,k} \rangle|$ in mBZ for (a-d) $n = 0, 1, 2, 3$ at $\theta = 2.13^\circ$ and (e-h) $n = 0, 1, 2, 3$ at $\theta = 3.89^\circ$. The arrows indicate the data range in each plot.

first moiré band. The θ dependence of the generalized LL weights is further reflected in momentum space, as illustrated in Fig. 5. This figure displays $|c_{2,n,k}^{(+)}|$ for $n = 0-3$ at $\theta = 2.13^\circ$ and 3.89° , corresponding to Chern numbers $\mathcal{C} = +1$ and -1 , respectively, for the second moiré band. These amplitudes share the same symmetries as $|c_{1,n,k}^{(s)}|$ in Fig. 3, including threefold rotational symmetry and invariance under $k_y \rightarrow -k_y$. At $\theta = 2.13^\circ$, the dominant component $|c_{2,1,k}^{(+)}|$ is above 0.94 across the mBZ, indicating an adiabatic connection between $\psi_{+,2,k}(r)$ and the generalized 1LL. In contrast, no single component dominates at $\theta = 3.89^\circ$ for every momentum, confirming that $\psi_{+,2,k}(r)$ becomes topologically distinct. In particular, at the γ point, $|c_{2,3,k}^{(+)}|$ is dominant and reaches 0.9, whereas $|c_{2,1,k}^{(+)}|$ vanishes; away from γ , $|c_{2,1,k}^{(+)}|$ becomes dominant, approaching unity at κ_{\pm} .

V. ABELIAN FRACTIONALIZED STATES

We investigate the many-body effects within the first moiré band. Given its close similarity to the generalized 0LL, Abelian fractionalized states can be expected. The many-body Hamiltonian projected onto the first band is given by,

$$\hat{\mathcal{H}}_1 = \mathcal{P}_1 \hat{H}^{(\text{full})} \mathcal{P}_1. \quad (20)$$

where $\hat{H}^{(\text{full})}$ is the full many-body Hamiltonian in the hole basis (see Appendix C for details). Here the subspace \mathcal{P}_1 is spanned by the many-body basis states where the first band at the $+K$ valley is partially occupied and

all other bands are empty in the hole basis,

$$\mathcal{P}_1 = \text{span} \left\{ \prod_{i=1}^{N_e} \varphi_{+,1,\mathbf{k}_i}^\dagger |0\rangle, \mathbf{k}_i \in \text{mBZ} \right\}, \quad (21)$$

where $\varphi_{\tau,n,\mathbf{k}}^\dagger$ ($\varphi_{\tau,n,\mathbf{k}}$) denotes the hole creation (annihilation) operator of a Bloch state at momentum \mathbf{k} , n th band and valley τ , N_e is the number of doped holes and $|0\rangle$ is the vacuum state corresponding to no doped holes in tMoTe₂. We assume full valley polarization for the doped holes in the projected Hamiltonian $\hat{\mathcal{H}}_1$, which can be further formulated as,

$$\begin{aligned} \hat{\mathcal{H}}_1 = & \sum_{\mathbf{k}} (-\mathcal{E}_{+,1,\mathbf{k}}) \varphi_{+,1,\mathbf{k}}^\dagger \varphi_{+,1,\mathbf{k}} \\ & + \sum_{\mathbf{k}_1 \mathbf{k}_2 \mathbf{k}_3 \mathbf{k}_4} V_{\mathbf{k}_1 \mathbf{k}_2 \mathbf{k}_3 \mathbf{k}_4} \varphi_{+,1,\mathbf{k}_1}^\dagger \varphi_{+,1,\mathbf{k}_2}^\dagger \varphi_{+,1,\mathbf{k}_3} \varphi_{+,1,\mathbf{k}_4}, \end{aligned} \quad (22)$$

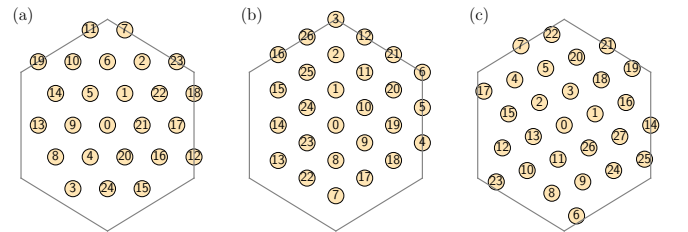


FIG. 6. (a-b) The 25-, 27-, and 28-unit-cell momentum clusters used in the ED calculations. The circled numbers are momentum indices.

The interaction matrix element $V_{\mathbf{k}_1 \mathbf{k}_2 \mathbf{k}_3 \mathbf{k}_4}$ is given by

$$V_{\mathbf{k}_1 \mathbf{k}_2 \mathbf{k}_3 \mathbf{k}_4} = \frac{1}{2\mathcal{A}} \sum_{\mathbf{q}} V(\mathbf{q}) M_{\mathbf{k}_1 \mathbf{k}_4}^{+11}(\mathbf{q}) M_{\mathbf{k}_2 \mathbf{k}_3}^{+11}(-\mathbf{q}), \quad (23)$$

where \mathcal{A} is the system area, $V_{\mathbf{q}} = 2\pi e^2/(\epsilon|\mathbf{q}|)$ is the Coulomb interaction with ϵ the dielectric constant, and we set $\epsilon = 5$ in this work. The plane-wave matrix element $M_{\mathbf{k}\mathbf{k}'}^{\tau nn'}(\mathbf{q})$ is defined as

$$M_{\mathbf{k}\mathbf{k}'}^{\tau nn'}(\mathbf{q}) = \int d\mathbf{r} e^{i\mathbf{q}\cdot\mathbf{r}} [f_{\tau, n, \mathbf{k}}(\mathbf{r})]^* f_{\tau, n', \mathbf{k}'}(\mathbf{r}), \quad (24)$$

where $f_{\tau, n, \mathbf{k}}(\mathbf{r})$ denotes the Bloch wave function. In Eq. (24), we take $f_{+,1,\mathbf{k}}(\mathbf{r})$ to be $[\psi_{+,1,\mathbf{k}}(\mathbf{r})]^*$ and $[\Theta_{0,\mathbf{k}}^{(+)}(\mathbf{r})]^*$, which we refer to as the original model and the variational model, respectively. Here $\psi_{+,1,\mathbf{k}}(\mathbf{r})$ is the Bloch wave function for the first moiré band of the single particle Hamiltonian H_+ in Eq. (9), and $\Theta_{0,\mathbf{k}}^{(+)}(\mathbf{r})$ is the generalized 0LL wave function variationally obtained in Section IV A. The complex conjugation is taken to implement the particle-hole transformation, as we work in the hole basis.

We perform exact diagonalization (ED) for the projected Hamiltonian $\hat{\mathcal{H}}_1$. Our study focuses on hole fillings $\nu_h = 1/3$ and $2/5$, which belong to the Jain sequence $\nu_h = p/(2p+1)$ with $p = 1, 2$, as well as their particle-hole conjugates $\nu_h = 2/3$ and $3/5$. The ED calculations are carried out on a 27-unit-cell cluster for $\nu_h = 1/3$ and $2/3$, and on a 25-unit-cell cluster for $\nu_h = 2/5$ and $3/5$. In Figs. 6(a) and 6(b) we show the geometries of these clusters in the momentum space. In Fig. 7, the left panels show the ED spectra for both models at $\theta = 3.15^\circ$, which exhibit quantitative agreement and clearly reveal the characteristics of Abelian-type FCIs at the Jain sequences. Specifically, the threefold quasi-degenerate ground states appear at zero momentum for $\nu_h = 1/3$ and $2/3$, and fivefold quasi-degenerate ground states appear at zero momentum for $\nu_h = 2/5$ and $3/5$, which are separated from excited states by a finite gap.

We present the twist angle dependence of the charge-neutral gap E_g and ground state energy spread E_s in the right panels of Fig. 7. We define the charge-neutral gap as $E_g = E_{n+1} - E_n$ and the ground-state energy spread as $E_s = E_n - E_1$, where E_i is the i -th lowest energy level. We set $n = 3$ for $\nu_h = 1/3$ and $2/3$, and $n = 5$ for $\nu_h = 2/5$ and $3/5$. The numerical results can be summarized as follows. (1) At $\nu_h = 2/3$, E_g is significantly larger than E_s within $\theta \in [2.13^\circ, 3.89^\circ]$, suggesting a stable FCI. Furthermore, E_g grows with increasing θ , which can be attributed to the enhancement of the characteristic interaction energy scale $e^2/(\epsilon a_M)$. (2) At $\nu_h = 1/3$, the FCI phase is stable only in a narrower twist-angle window, $\theta \in [2.45^\circ, 3.48^\circ]$, as characterized by a finite E_g . Beyond this region, the gap closes at $\theta = 3.89^\circ$ due to the increasing single-particle bandwidth, while the system transitions into a CDW state at $\theta = 2.13^\circ$. The CDW phase is characterized by a

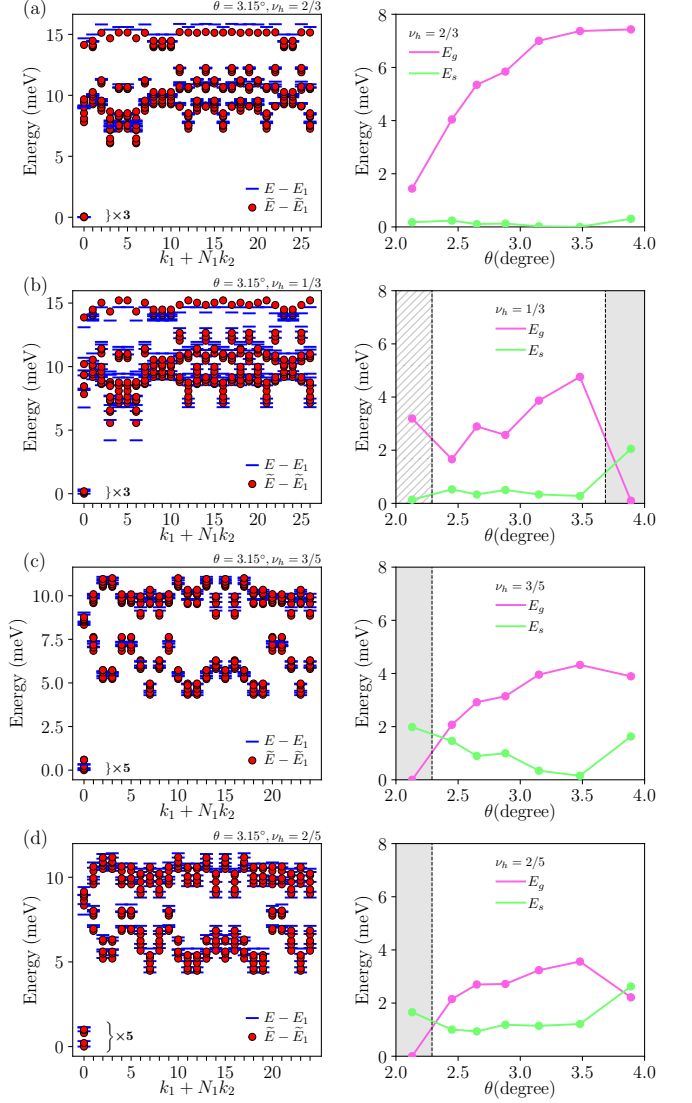


FIG. 7. (a-d) ED results at $\nu_h = 2/3, 1/3, 3/5$, and $2/5$. Left panels, ED spectrum of the original model (blue lines) and variational model (red dots) at $\theta = 3.15^\circ$. Right panels, The energy gap E_g (pink) and spread E_s (green) as functions of θ based on the original model. Gray regions mark the gapless phase, while the hatched region denotes the CDW phase.

threefold quasi-degenerate ground state across momentum sectors at the mBZ center and corners, a transition driven by enhanced spatial variation of the single-particle wave functions. (3) At $\nu_h = 3/5$ and $2/5$, the FCI phase remains stable within $\theta \in [2.45^\circ, 3.89^\circ]$, as evidenced by a finite energy gap E_g . The system becomes gapless below this range at $\theta = 2.13^\circ$.

We also examine fillings $\nu_h = 3/7$ and $4/9$, which belong to the Jain sequence $\nu_h = p/(2p+1)$ with $p = 3, 4$, as well as their particle-hole conjugates $\nu_h = 4/7$ and $5/9$. The ED calculations are carried out on a 28-unit-cell cluster for $\nu_h = 3/7$ and $4/7$, and on a 27-unit-cell cluster for $\nu_h = 4/9$ and $5/9$, with momentum clusters shown

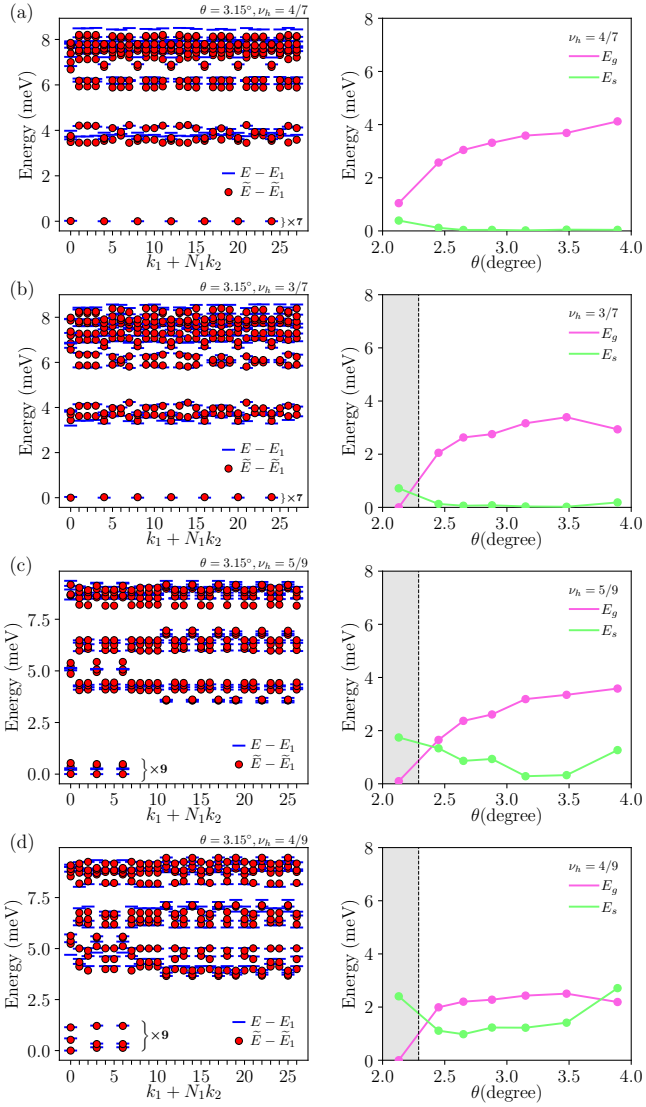


FIG. 8. (a-b) ED results at $\nu_h = 4/7, 3/7, 5/9$, and $4/9$. Left panels, ED spectrum of the original model (blue lines) and variational model (red dots) at $\theta = 3.15^\circ$. Right panels, The energy gap E_g (pink) and spread E_s (green) as functions of θ based on the original model. Gray regions mark the gapless phase.

in Fig. 6. In Fig. 8, the left panels show the ED spectra for the original and variational models at $\theta = 3.15^\circ$, which exhibit quantitative agreement and clearly reveal the characteristics of Abelian-type FCIs at the Jain sequences. These features are evidenced by the sevenfold quasi-degenerate ground states appear for $\nu_h = 3/7$ and $4/7$, and ninefold quasi-degenerate ground states appear for $\nu_h = 4/9$ and $5/9$, which are separated from excited states by a finite gap.

We show E_g and E_s as a function of θ in the right panels of Fig. 8, where we set $n = 7$ for $\nu_h = 3/7$ and $4/7$, and $n = 9$ for $\nu_h = 4/9$ and $5/9$. At $\nu_h = 4/7$, E_g is significantly larger than E_s within $\theta \in [2.13^\circ, 3.89^\circ]$,

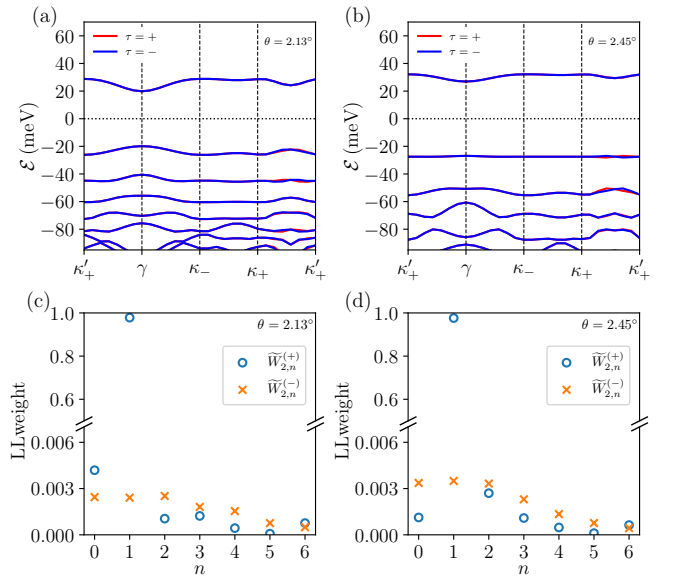


FIG. 9. (a-b) HF band structure presented in the electron basis. Filling factor ν_h is 2 and twist angle θ is 2.13° and 2.45° . The bands in τK valley are plotted by red and blue lines for $\tau = +$ and $-$, respectively. The horizontal dotted line mark the Fermi energy in the gap. (c-d) LL weights $\tilde{W}_{2,n}^{(s)}$ at 2.13° and 2.45° .

suggesting a stable FCI. At $\nu_h = 3/7$ and $5/9$, the FCI phase remains stable with a finite energy gap E_g for $\theta \in [2.45^\circ, 3.89^\circ]$, and the system becomes gapless below this range at $\theta = 2.13^\circ$. At $\nu_h = 4/9$, E_g is finite but comparable to E_s for $\theta \in [2.45^\circ, 3.89^\circ]$, indicating that the FCI phase is less robust. Additionally, we perform ED calculations at $\nu_h = 1/2$. The ED spectra at $\nu_h = 1/2$ mimics that of the zeroth LL for all twist angles under study, indicating a composite Fermi liquid state (see Appendix D for details).

The asymmetry between the FCI states at $\nu_h = p/(2p+1)$ and $(p+1)/(2p+1)$ arises from the lack of particle-hole symmetry in the first band of tMoTe₂, stemming from its finite bandwidth and momentum-dependent quantum geometric tensor, in contrast to conventional Landau levels. As a general trend, we find that FCI states in the range $1/2 < \nu_h < 1$ are more robust than their particle-hole conjugates at $\nu_h < 1/2$, as evidenced by their larger gaps.

VI. NONABELIAN FRACTIONALIZED STATE

The close similarity between the second band of tMoTe₂ and the generalized 1LL at $\theta = 2.13^\circ$ suggests that tMoTe₂ may provide a viable platform for realizing a non-Abelian phase. Motivated by this connection, we focus on $\nu_h = 5/2$, a candidate filling factor for stabilizing the MR state. A multi-band ED analysis at this filling, however, is computationally prohibitive. To ad-

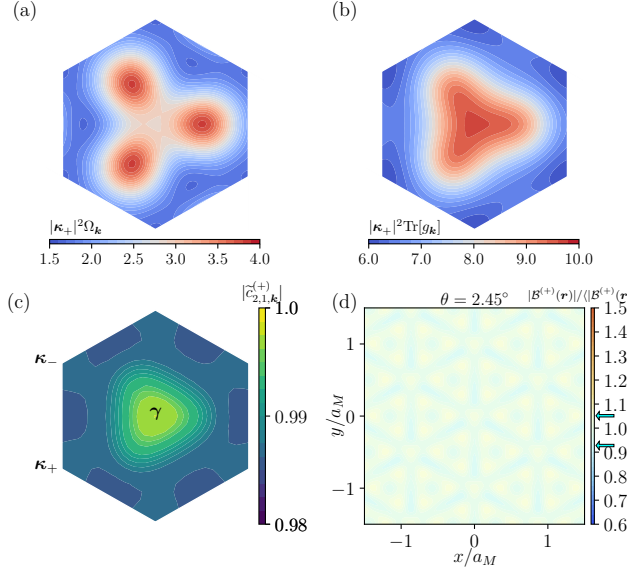


FIG. 10. (a-b) Berry curvature $\Omega_{\mathbf{k}}$ and trace of quantum metric $\text{Tr}[g_{\mathbf{k}}]$ in the mBZ for the second HF band in $+K$ valley. (c) Overlap $|\tilde{c}_{2,1,\mathbf{k}}^{(+)}|$. (d) Map of $|\mathcal{B}^{(+)}(\mathbf{r})|$ scaled by its spatial average. In all plots, $\theta = 2.45^\circ$.

dress this challenge, we first carry out a self-consistent HF calculation at $\nu_h = 2$, which allows us to construct a refined Bloch basis renormalized by interactions.

Using this refined basis, we then build the effective many-body Hamiltonian at $\nu_h = 5/2$ by treating the first renormalized band in both valleys as inert and considering a half-filled second band in the $+K$ valley, assuming spontaneous valley polarization. This Hamiltonian is subsequently studied using ED, and the resulting energy spectrum and PES are analyzed to assess whether the system exhibits features consistent with the MR phase.

A. HF Renormalized Bands

We first perform HF calculation at $\nu_h = 2$, approximating the interaction effects via corrections to the single-particle orbitals (described in Appendix C). This yields a corrected Bloch wave function, denoted as $[\tilde{\psi}_{\tau,n,\mathbf{k}}(\mathbf{r})]^*$ in the hole basis. The corresponding creation and annihilation operators are $\tilde{\varphi}_{\tau,n,\mathbf{k}}^\dagger$ and $\tilde{\varphi}_{\tau,n,\mathbf{k}}$.

Figures 9(a) and 9(b) show the HF band structure at $\nu_h = 2$ with twist angle $\theta = 2.13^\circ$ and $\theta = 2.45^\circ$, respectively. In both cases, the top four moiré bands in the electron basis are isolated from each other and exhibit narrow bandwidths. All of these bands possess a quantized Chern number $\mathcal{C} = +1$ in the $+K$ valley. The quantum weight \mathcal{K} of the n th topmost band for $n = 1$ to 4 is 1.03, 3.08, 5.17, and 7.37 at $\theta = 2.13^\circ$, and 1.02, 3.08, 5.18, and 7.45 at $\theta = 2.45^\circ$, respectively. The deviation between the n th band and the generalized $(n-1)$ LL Landau level, quantified by $\mathcal{K} - (2n-1)|\mathcal{C}|$, remains below

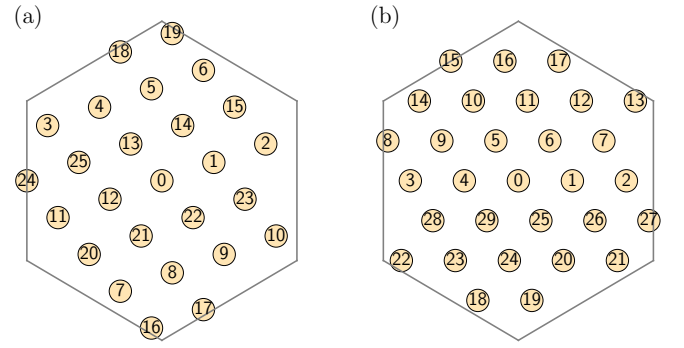


FIG. 11. (a-b) The 26- and 30-unit-cell momentum clusters used in the ED calculations. The circled numbers are momentum indices.

0.5 for all four bands. This suggests a series of LL-like bands after the HF correction.

Focusing on the second band, the corresponding quantum geometric quantities at $\theta = 2.45^\circ$, namely, $\Omega_{\mathbf{k}}$ and $\text{Tr}[g_{\mathbf{k}}]$, are displayed, respectively, in Figs. 10(a) and 10(b), both exhibiting strong momentum dependence. Nevertheless, the indicator $\mathcal{K} - 3|\mathcal{C}|$ takes a small value of 0.08, reduced compared to its noninteracting value of 0.50. This reduction has also been observed in Ref. 43. The renormalized bandwidth is 1.3 meV at $\theta = 2.45^\circ$, which is smaller than the noninteracting value, and increases to 6.3 meV at $\theta = 2.13^\circ$.

We further perform the variational mapping between the Bloch wave function $\tilde{\psi}_{+,2,\mathbf{k}}(\mathbf{r})$ and the generalized 1LL. The dominant weight is chosen as $\widetilde{W}_{2,1}^{(+)}$, where we define

$$\widetilde{W}_{m,n}^{(s)} = \frac{1}{N} \sum_{\mathbf{k}} |\tilde{c}_{m,n,\mathbf{k}}^{(s)}|^2, \quad (25)$$

and $\tilde{c}_{m,n,\mathbf{k}}^{(s)} = \langle \Theta_{n,\mathbf{k}}^{(s)} | \tilde{\psi}_{+,m,\mathbf{k}} \rangle$. Following the procedure described in Section IV, we variationally adjust $\mathcal{B}^{(+)}(\mathbf{r})$ in $\Theta_{n,\mathbf{k}}^{(+)}(\mathbf{r})$ to maximize $\widetilde{W}_{2,1}^{(+)}$. Figures 9(c) and 9(d) present the resulting generalized LL weight $\widetilde{W}_{2,n}^{(s)}$ of the second band at $\theta = 2.13^\circ$ and $\theta = 2.45^\circ$, respectively. The dominant weight $\widetilde{W}_{2,1}^{(+)}$ reaches 0.97 at both twist angles—larger than its noninteracting value—while all other weights are smaller by two orders of magnitude. At $\theta = 2.45^\circ$, the overlap between $\tilde{\psi}_{+,2,\mathbf{k}}(\mathbf{r})$ and the generalized 1LL wave function, $|\tilde{c}_{2,1,\mathbf{k}}^{(+)}|$, exceeds 0.98 across the entire mBZ, as shown in Fig. 10(c). We also display the map of $|\mathcal{B}^{(+)}(\mathbf{r})|$ in Fig. 10(d), which exhibits suppressed fluctuations relative to the generalized 1LL calculated from the noninteracting wave function $\psi_{+,2,\mathbf{k}}(\mathbf{r})$, as shown in Fig. 4(d).

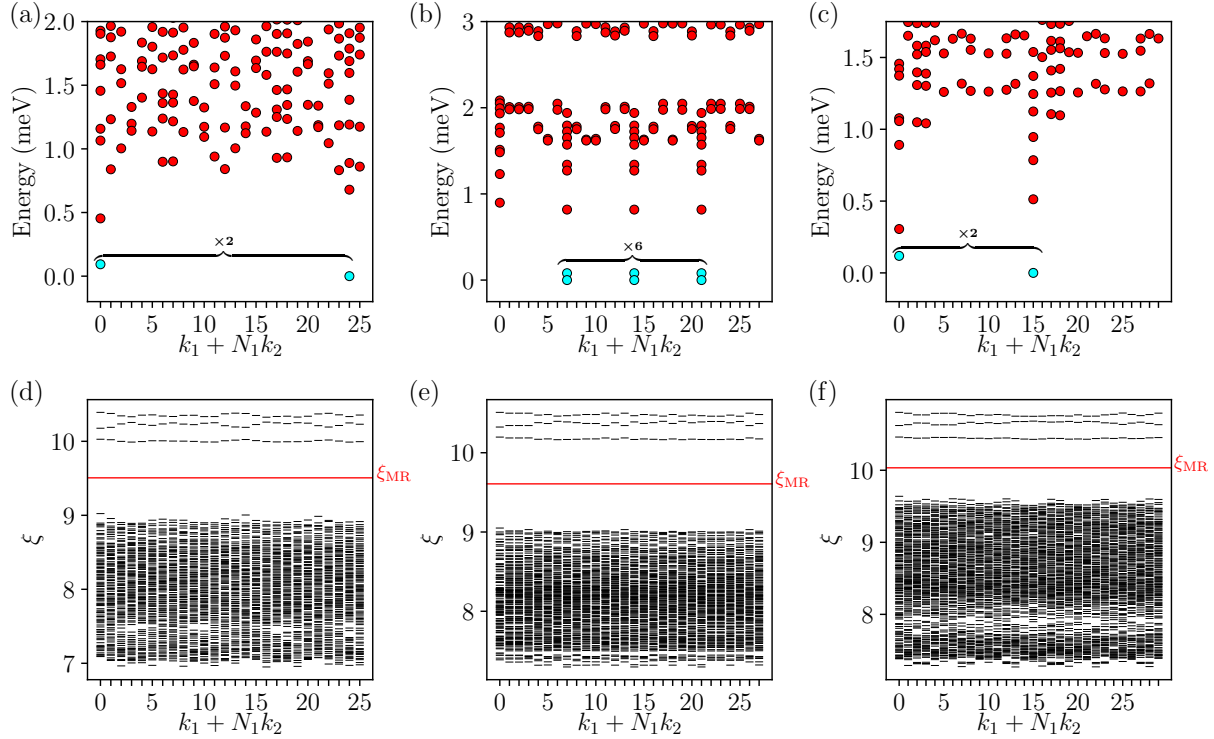


FIG. 12. (a-c) ED spectrum at $\nu_h = 5/2$ and $\theta = 2.45^\circ$, obtained with $N = 26, 28$, and 30 clusters. The quasi-degenerate states are highlighted in cyan. (d-f) PES with $N_A = 3$ for the quasi-degenerate states highlighted in cyan in (a-c).

B. ED Calculation

We now carry out ED studies at $\nu_h = 5/2$ in the projected many-body Hamiltonian,

$$\hat{\mathcal{H}}_2 = \mathcal{P}_2 \hat{H}^{(\text{full})} \mathcal{P}_2. \quad (26)$$

Here \mathcal{P}_2 is spanned by the many-body basis states where the first band is completely filled and the second band is partially occupied at $+K$ valley,

$$\mathcal{P}_2 = \text{span}\left\{\prod_{i=1}^{N'_e} \tilde{\varphi}_{+,2,\mathbf{k}_i}^\dagger \prod_{\tau=\pm} \prod_{j=1}^N \tilde{\varphi}_{\tau,1,\mathbf{k}_j}^\dagger |0\rangle, \mathbf{k}_i \in \text{mBZ}\right\}, \quad (27)$$

N is the number of momentum points (unit cells) in the momentum (real) space, $N'_e = N/2$ is the number of holes in the second band, and $N'_e + 2N$ is the total number of holes. $\hat{\mathcal{H}}_2$ is formulated as,

$$\hat{\mathcal{H}}_2 = \sum_{\mathbf{k}} (-\lambda_w \tilde{\mathcal{E}}_{+,2,\mathbf{k}}) \tilde{\varphi}_{+,2,\mathbf{k}}^\dagger \tilde{\varphi}_{+,2,\mathbf{k}} + \hat{V} + E_1, \quad (28)$$

where $-\tilde{\mathcal{E}}_{+,2,\mathbf{k}}$ is the HF corrected band energy in the hole basis and E_1 denotes the total energy of the filled first band. We introduce a parameter λ_w to phenomenologically tune the bandwidth. In $\hat{\mathcal{H}}_2$, \hat{V} is the interaction

term projected onto the second band,

$$\hat{V} = \sum_{\mathbf{k}_1 \mathbf{k}_2 \mathbf{k}_3 \mathbf{k}_4} \tilde{V}_{\mathbf{k}_1 \mathbf{k}_2 \mathbf{k}_3 \mathbf{k}_4} \tilde{\varphi}_{+,2,\mathbf{k}_1}^\dagger \tilde{\varphi}_{+,2,\mathbf{k}_2}^\dagger \tilde{\varphi}_{+,2,\mathbf{k}_3} \tilde{\varphi}_{+,2,\mathbf{k}_4}. \quad (29)$$

The interaction matrix element $\tilde{V}_{\mathbf{k}_1 \mathbf{k}_2 \mathbf{k}_3 \mathbf{k}_4}$ is given by

$$\tilde{V} = \frac{1}{2\mathcal{A}} \sum_{\mathbf{q}} V(\mathbf{q}) \tilde{M}_{\mathbf{k}_1 \mathbf{k}_4}^{+22}(\mathbf{q}) \tilde{M}_{\mathbf{k}_2 \mathbf{k}_3}^{+22}(-\mathbf{q}), \quad (30)$$

and the plane-wave matrix element is

$$\tilde{M}_{\mathbf{k}\mathbf{k}'}^{+22}(\mathbf{q}) = \int d\mathbf{r} e^{i\mathbf{q}\cdot\mathbf{r}} [\tilde{f}_{+,2,\mathbf{k}}(\mathbf{r})]^* \tilde{f}_{+,2,\mathbf{k}'}(\mathbf{r}), \quad (31)$$

and we take the wave function $\tilde{f}_{+,2,\mathbf{k}}(\mathbf{r})$ to be $[\tilde{\psi}_{+,2,\mathbf{k}}(\mathbf{r})]^*$ unless otherwise stated.

We perform ED calculations using clusters of sizes $N = 26, 28$, and 30 , where the corresponding momentum clusters are depicted in Fig. 11. To reduce finite-size effects, the preceding HF calculations are carried out on enlarged clusters with $234, 252$, and 270 unit cells, respectively—each exactly nine times the size of the corresponding ED cluster.

We focus on the twist angle $\theta = 2.45^\circ$, where the second moiré band is particularly narrow. Figures 12(a-c) presents the corresponding ED spectra. The quasi-degenerate ground states are observed in the three clusters. For the $N = 28$ cluster, the ground manifold is

sixfold quasi-degenerate and gapped, while the $N = 26$ and $N = 30$ clusters exhibit a twofold quasi-degeneracy and also gapped. This dependence of the ground-state degeneracy on the parity of the electron number $N'_e = N/2$ —sixfold for even and twofold for odd—is a characteristic signature of the MR phase [10]. Moreover, the momentum sectors in which these ground states appear agree with the predictions of the generalized Pauli principle for the MR state [75, 76]. Specifically, the two nearly degenerate ground states for the $N = 26$ ($N = 30$) cluster appear at momentum indices 0 and 24 (15), corresponding respectively to the mBZ center and the midpoint of the mBZ edge. For the $N = 28$ cluster, the six quasi-degenerate ground states occur at momentum indices 7, 14, and 21 (midpoints of the mBZ edges), with each sector hosting a pair of states. The correspondence between momenta and their indices is shown in Fig. 11.

To further probe the nature of the states, we examine the PES, a method capable of distinguishing the MR state from competing states [77]. The PES is constructed by dividing the system into two subsystems A and B , containing N_A and N_B particles, respectively [42, 78]. The reduced density matrix $\hat{\rho}_A$ of subsystem A is defined as the average over all reduced density matrices $\hat{\rho}_{m,A}$ for the m th quasi-degenerate ground state $|\Psi_m\rangle$,

$$\hat{\rho}_A = \frac{1}{N_{\text{GS}}} \sum_{m=1}^{N_{\text{GS}}} \hat{\rho}_{m,A}, \quad (32)$$

where N_{GS} is the quasi-degeneracy. $\hat{\rho}_{m,A}$ is obtained by tracing out the degrees of freedom of subsystem B from the density matrix $\hat{\rho}_m$

$$\hat{\rho}_{m,A} = \text{Tr}_B(\hat{\rho}_m), \hat{\rho}_m = |\Psi_m\rangle \langle \Psi_m|. \quad (33)$$

PES is then calculated from

$$\hat{\rho}_A = \sum_n e^{-\xi_{A,n}} |\alpha_{A,n}\rangle \langle \alpha_{A,n}|, \quad (34)$$

where $|\alpha_{A,n}\rangle$ is the eigenstate of $\hat{\rho}_A$ and $\xi_{A,n}$ is PES in the n th level. We take $N_A = 3$ in the calculation. Figures 12(d-f) show PES for the quasi-degenerate states in the three clusters as a function of total momentum of particles in subsystem A . We find a significant entanglement gap at ξ_{MR} separating the spectrum in all three cases, with the low-lying levels exhibiting counting patterns that match the quasi-hole excitations for the MR state. For $N_A = 3$, the counts are 2522, 3192, and 3970 for the $N = 26, 28$, and 30 clusters, respectively [79]. Therefore, both the ED spectrum and the PES consistently indicate a MR state.

The correspondence between the second moiré band and a generalized first Landau level enables an adiabatic link between the MR state in tMoTe₂ at $\theta = 2.45^\circ$ and that in the generalized 1LL. Through this link, the state can be continuously deformed into the MR state of the standard first LL. To this end, we use exact diagonalization to study a family of Hamiltonians that are continuously interpolated through three successive stages, with each stage controlled by a single tuning parameter.

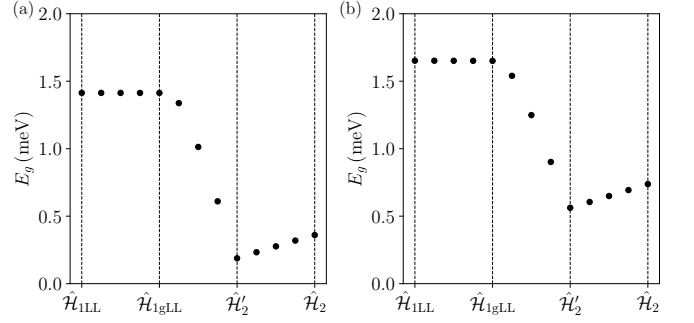


FIG. 13. The energy gap E_g calculated for a series of interpolated Hamiltonians between the second band of tMoTe₂ at $\theta = 2.45^\circ$ and the first Landau level. Results are shown for (a) the $N = 26$ cluster and (b) the $N = 28$ cluster. The labels on the horizontal axis— $\hat{H}_{1\text{LL}}$, $\hat{H}_{1\text{gLL}}$, \hat{H}'_2 , and \hat{H}_2 —correspond to the Hamiltonian of the first LL, the generalized 1LL, and the original tMoTe₂ model, respectively.

Firstly, we set $\lambda_w = 0$ and take the wave function $\tilde{f}_{+,2,\mathbf{k}}(\mathbf{r})$ to be $[\Theta_{1,\mathbf{k}}^{(+)}(\mathbf{r})]^*$ in Eq. (31). We then introduce a parameter $\lambda_B \in [0, 1]$ to continuously interpolate the spatial fluctuations of $|\mathcal{B}^{(+)}(\mathbf{r})|^2$ via:

$$|\mathcal{B}^{(+)}(\mathbf{r}, \lambda_B)|^2 = \lambda_B |\mathcal{B}^{(+)}(\mathbf{r})|^2 + (1 - \lambda_B) \mathcal{B}_0^2, \quad (35)$$

where \mathcal{B}_0^2 denotes the spatial average of $|\mathcal{B}^{(+)}(\mathbf{r})|^2$. At $\lambda_B = 0$, the Hamiltonian $\hat{H}_{1\text{LL}}$ describes a flat band with Coulomb interaction projected onto the standard first LL; at $\lambda_B = 1$, the Hamiltonian $\hat{H}_{1\text{gLL}}$ corresponds to a flat band with Coulomb interaction projected onto the generalized 1LL.

Secondly, we maintain $\lambda_w = 0$ and $\lambda_B = 1$, but introduce $\lambda_F \in [0, 1]$ that tunes the weight of the generalized 1LL in the wave function. The wave function $\tilde{f}_{+,2,\mathbf{k}}(\mathbf{r})$ is taken as

$$\tilde{f}_{+,2,\mathbf{k}}(\mathbf{r}) = \tilde{\mathcal{N}}_{\mathbf{k}} \{ \lambda_F [\tilde{\psi}_{+,2,\mathbf{k}}(\mathbf{r})]^* + (1 - \lambda_F) [\Theta_{1,\mathbf{k}}^{(+)}(\mathbf{r})]^* \}, \quad (36)$$

where $\tilde{\mathcal{N}}_{\mathbf{k}}$ is a normalization factor. At $\lambda_F = 0$, the corresponding Hamiltonian is $\hat{H}_{1\text{gLL}}$; at $\lambda_F = 1$, the Hamiltonian is denoted as \hat{H}'_2 . Here, we choose a gauge in which the overlap $\langle \Theta_{1,\mathbf{k}}^{(+)} | \tilde{\psi}_{+,2,\mathbf{k}} \rangle$ is real and positive, ensuring that $\tilde{f}_{+,2,\mathbf{k}}(\mathbf{r})$ varies smoothly with λ_F .

Finally, we reintroduce the bandwidth of the second moiré band by tuning $\lambda_w \in [0, 1]$, which allows us to interpolate between \hat{H}'_2 and the original Hamiltonian \hat{H}_2 .

Figure 13 presents the evolution of the many-body gap E_g extracted from the ED spectra. For the $N = 26$ and $N = 28$ clusters, we define the gap as $E_g = E_3 - E_2$ and $E_g = E_7 - E_6$, respectively, where E_i denotes the i th lowest energy level. The gap remains finite throughout the interpolation, establishing adiabatic continuity along the entire path. In particular, E_g is nearly unchanged between $\hat{H}_{1\text{LL}}$ and $\hat{H}_{1\text{gLL}}$, consistent with the weak spatial

modulation of the function $\mathcal{B}(\mathbf{r})$ as shown in Fig. 10(d). By contrast, the gap decreases rapidly as the 1LL weight is reduced from unity in \mathcal{H}_{1gLL} to 0.97 in \mathcal{H}'_2 , highlighting the strong sensitivity of the MR state to the detailed structure of the underlying wave functions. Remarkably, introducing a finite bandwidth when interpolating from \mathcal{H}'_2 to \mathcal{H}_2 slightly enhances the gap. Upon further increasing λ_w , the gap eventually closes at $\lambda_w \approx 8$ for the 26 cluster and at $\lambda_w \approx 11$ for the 30 cluster. This behavior underscores the nontrivial role of bandwidth in stabilizing non-Abelian topological states.

Given that the second moiré miniband resembles the first LL, it is natural to ask whether the \mathbb{Z}_3 Read-Rezayi (RR) state could be stabilized. Similar to the MR state at $\nu = 5/2$, the RR state can appear at fillings $\nu = 12/5$ and $\nu = 13/5$ in LLs and exhibit quasiparticle excitations that obey non-Abelian statistics [80]. Crucially, the RR state is predicted to support Fibonacci anyons, which are capable of universal topological quantum computation [81]. However, in our ED calculations for fillings $\nu_h = 12/5$ and $13/5$ in tMoTe₂ at $\theta = 2.45^\circ$ —corresponding to fillings $2/5$ and $3/5$ in the second moiré band—we do not find clear signatures of the RR phase. This is consistent with the known difficulty of stabilizing the RR state even in the standard first LL, where it typically requires specific, finely-tuned interactions [43, 82]. In addition, we perform ED calculation for fillings $\nu_h = 7/3$ and $8/3$ in tMoTe₂ at $\theta = 2.45^\circ$ in a 27-unit-cell cluster, corresponding to fillings $1/3$ and $2/3$ in the second moiré band. The ED results, within the projected Hilbert space in Eq. (27), indicate a CDW phase at $\nu_h = 7/3$, whereas a Laughlin-type FCI is stabilized at $\nu_h = 8/3$. We note that the conventional 1LL can support Laughlin-type fractionalized states, which provide a clear example that the trace condition $\mathcal{K} = |\mathcal{C}|$ is not a necessary requirement for the existence of fractionalized states.

Motivated by the similarly large generalized 1LL weight of the second band at $\theta = 2.13^\circ$, we extend our numerical calculations to this twist angle (see Appendix E for details). The ED spectra and PES at $\nu_h = 5/2$ point toward a CDW state rather than a MR phase. A key factor influencing the competition between CDW and MR states appears to be the bandwidth. The phase diagram in the (λ_F, λ_w) parameter space suggests that the larger bandwidth at $\theta = 2.13^\circ$ tends to destabilize the MR phase and favors the CDW state.

VII. DISCUSSION

In summary, we develop a theoretical framework for decomposing Chern bands into generalized Landau levels and use it to investigate Abelian and non-Abelian fractionalized states in tMoTe₂. Specifically, we employ a variational mapping to express the Bloch states of the first two moiré Chern bands in terms of generalized LLs, providing a clear perspective on how these fractionalized states emerge. The first moiré band is found to be dom-

inated by the generalized 0LL, naturally leading to the formation of Abelian FCIs in the Jain sequences.

For the second moiré band, HF calculations at hole filling $\nu_h = 2$ reveal a dominant generalized 1LL component at $\theta = 2.13^\circ$ and $\theta = 2.45^\circ$, which in turn motivates our study of interaction-driven phases at fractional fillings. Importantly, this identification is nontrivial: although the quantum weight \mathcal{K} of the second band lies close to the nominal value $3|\mathcal{C}|$, such proximity alone does not a priori ensure a generalized 1LL-like wave function. Our explicit decomposition demonstrates that resolving the internal generalized-LL structure is essential for unambiguously establishing the 1LL-like nature of the band. Exact diagonalization calculations at $\nu_h = 5/2$ identify the evidence of the non-Abelian MR state at $\theta = 2.45^\circ$ in both the energy spectra and the PES. This MR state is further verified by its adiabatic connection to the corresponding state in the first LL. We also perform systematic numerical calculation at $\theta = 2.13^\circ$, where a competition between the MR state and CDW state is found, with the transition primarily controlled by the bandwidth (See Appendix E for details). These results demonstrate a quantitative correspondence between moiré Chern bands and generalized LLs, establishing a foundation for understanding the emergence of fractionalized topological phases in moiré systems.

We compare our numerical results with available experiments. For fractionalized states at $\nu_h < 1$, our calculations predict FCIs in the Jain sequences at $\nu_h = 1/3, 2/3, 2/5, 3/5, 3/7, 4/7, 5/9$, and $4/9$ across a broad range of twist angles. Transport measurements have indeed observed fractional quantum anomalous Hall effects in tMoTe₂ at $\nu_h = 2/3, 3/5$, and $4/7$ down to zero external magnetic field [17, 19, 20, 69, 70, 83], as well as at $\nu_h = 5/9$ under a finite magnetic field (~ 0.5 T), whereas no such signatures have been reported for $\nu_h < 1/2$ [83]. This discrepancy may arise from intrinsic effects, where fractionalized states at $\nu_h < 1/2$ are less robust or absent, or from extrinsic factors such as disorder and contact limitations at low fillings. Optical probes, however, have revealed signatures of fractionalized states even below $\nu_h = 1/2$ in the Jain sequences [84, 85], supporting our numerical results. At $\nu_h = 5/2$, ferromagnetism has been experimentally observed [69–71], but evidence for non-Abelian fractionalized states remains absent. We note that disorder effects become more severe at small twist angles. Transport and optical experiments based on high-quality devices at $\nu_h = 5/2$, combined with tuning parameters such as twist angle and pressure, could provide a decisive test of the emergence of non-Abelian fractionalized phases in tMoTe₂. On the numerical side, our studies employ band-projected Hamiltonians aimed at capturing the low-energy physics. Remote bands could influence the competition between fractionalized and other competing states [86], highlighting the need for further quantitative studies that go beyond the band-projection approximation. These combined theoretical and experimental efforts are essential to fully resolve the stability

and nature of both Abelian and non-Abelian fractionalized phases in tMoTe₂ at various fillings.

More broadly, the generalized LL framework offers a systematic approach to decompose Bloch bands with arbitrary Chern numbers, as shown in Eq. (14). By examining how expansion coefficients $c_{m,n,\mathbf{k}}^{(s)}$ —which control quantum geometric properties like the Chern number C and quantum weight \mathcal{K} —affect the competition between fractionalized phases and competing orders, key design principles for realizing fractionalized topological phases can be established. This could also help understand the emergence of such phases in models where bands deviate from ideal quantum geometry or are even topologically trivial [87–90], paving the way for a unified framework of interaction-driven fractionalized states in moiré and other quantum materials.

VIII. ACKNOWLEDGMENTS

We thank Heqiu Li, Hui Liu, Yan Zhang, and Quansheng Wu for valuable discussions. This work was supported by National Key Research and Development Program of China (Grants No. 2022YFA1402400 and No. 2021YFA1401300), National Natural Science Foundation of China (Grants No. 12274333 and No. 12550404). The numerical calculations in this paper have been performed on the supercomputing system in the Supercomputing Center of Wuhan University.

Appendix A: LL wave function

We present a brief review of the magnetic Bloch wave function for the n th LL and discuss symmetry-imposed constraints for $\mathcal{B}^{(s)}(\mathbf{r})$. The magnetic Bloch wave function for the zeroth LL is given by

$$\begin{aligned}\Psi_{0,\mathbf{k}}^{(-)}(\mathbf{r}) &= \frac{1}{S_{\mathbf{k}}\ell} \sigma(z + iz_{\mathbf{k}}\ell^2) e^{-\frac{1}{4}|z_{\mathbf{k}}|^2\ell^2 - \frac{1}{4}|z|^2\ell^{-2} + \frac{i}{2}z_{\mathbf{k}}^*z}, \\ \Psi_{0,\mathbf{k}}^{(+)}(\mathbf{r}) &= [\Psi_{0,-\mathbf{k}}^{(-)}(\mathbf{r})]^*,\end{aligned}\quad (\text{A1})$$

where $z = x + iy$, $z_{\mathbf{k}} = k_x + ik_y$, $S_{\mathbf{k}}$ is a normalization factor, $\ell = \sqrt{A_0/(2\pi)}$, A_0 is the area of the (magnetic) unit cell, and $\sigma(z)$ is the modified Weierstrass sigma function [73] formulated as

$$\sigma(z) = ze^{\frac{\eta_1 z^2}{z_1}} \frac{\theta_1(v \mid \tau)}{v\theta_1'(0 \mid \tau)}, \quad (\text{A2})$$

where $\theta_1(v \mid \tau)$ is the Jacobi theta function, $v = \pi z/z_1$, $\eta_1 = z_1^*/(4\ell^2)$, $\tau = z_2/z_1$, and $z_j = a_{j,x} + ia_{j,y}$. Here $\mathbf{a}_{1,2}$ are primitive (magnetic) lattice vectors, and we take $\mathbf{a}_{1,2} = (\pm\frac{\sqrt{3}}{2}, \frac{1}{2})a_M$. Expression of $\theta_1(u \mid \tau)$ is

$$\theta_1(u \mid \tau) = - \sum_{n=-\infty}^{+\infty} e^{i\pi\tau(n+\frac{1}{2})^2} e^{2\pi i(n+1/2)(u+1/2)}. \quad (\text{A3})$$

The magnetic Bloch wavefunction for the n th LL is formulated as

$$\begin{aligned}\Psi_{n,\mathbf{k}}^{(-)}(\mathbf{r}) &= \frac{(a^{\dagger})^n}{\sqrt{n!}} \Psi_{0,\mathbf{k}}^{(-)}(\mathbf{r}), \\ \Psi_{n,\mathbf{k}}^{(+)}(\mathbf{r}) &= [\Psi_{n,-\mathbf{k}}^{(-)}(\mathbf{r})]^*,\end{aligned}\quad (\text{A4})$$

where a^{\dagger} and a denote, respectively, the raising and lowering operators

$$a^{\dagger} = i \frac{-2\ell\partial_z + z^*\ell^{-1}/2}{\sqrt{2}}, \quad a = i \frac{-2\ell\partial_{z^*} - \ell^{-1}z/2}{\sqrt{2}}. \quad (\text{A5})$$

$\Psi_{n,\mathbf{k}}^{(s)}(\mathbf{r})$ satisfies the following magnetic translational symmetry and point-group symmetry [63]

$$\begin{aligned}\Psi_{n,\mathbf{k}}^{(s)}(\mathbf{r} + \mathbf{a}_i) &= -e^{-is\frac{1}{2\ell^2}\mathbf{a}_i \times \mathbf{r}} e^{i\mathbf{k} \cdot \mathbf{a}_i} \Psi_{n,\mathbf{k}}^{(s)}(\mathbf{r}), \\ \Psi_{0,\gamma}^{(s)}(\hat{R}_{3z}\mathbf{r}) &= e^{-i\frac{2}{3}\pi s} \Psi_{0,\gamma}^{(s)}(\mathbf{r}), \\ \Psi_{0,\kappa_{\pm}}^{(s)}(\hat{R}_{3z}\mathbf{r}) &= \Psi_{0,\kappa_{\pm}}^{(s)}(\mathbf{r}), \\ \Psi_{0,\gamma}^{(s)}(\hat{R}_{2y}\mathbf{r}) &= -[\Psi_{0,\gamma}^{(s)}(\mathbf{r})]^*,\end{aligned}\quad (\text{A6})$$

where \hat{R}_{ni} represents the n -fold rotation around the i -axis.

We now derive the constraints on $\mathcal{B}^{(s)}(\mathbf{r})$ imposed by the symmetry properties of $\Theta_{n,\mathbf{k}}^{(s)}(\mathbf{r})$. $\Theta_{n,\mathbf{k}}^{(s)}(\mathbf{r})$ is the Bloch wave function satisfying the translational symmetry

$$\Theta_{n,\mathbf{k}}^{(s)}(\mathbf{r} + \mathbf{a}_i) = e^{i\mathbf{k} \cdot \mathbf{a}_i} \Theta_{n,\mathbf{k}}^{(s)}(\mathbf{r}), \quad (\text{A7})$$

and has a decomposition

$$\Theta_{n,\mathbf{k}}^{(s)}(\mathbf{r}) = \mathcal{B}^{(s)}(\mathbf{r}) \xi_{\mathbf{k}}(\mathbf{r}), \quad (\text{A8})$$

where $\xi_{\mathbf{k}}(\mathbf{r})$ is a linear combination of $\Psi_{m,\mathbf{k}}^{(s)}(\mathbf{r})$. As a consequence, $\mathcal{B}^{(s)}(\mathbf{r})$ is constrained by the translational symmetry,

$$\mathcal{B}^{(s)}(\mathbf{r} + \mathbf{a}_i) = -e^{is\frac{1}{2\ell^2}\mathbf{a}_i \times \mathbf{r}} \mathcal{B}^{(s)}(\mathbf{r}). \quad (\text{A9})$$

In the case of tMoTe₂, The C_{3z} and $C_{2y}\mathcal{T}$ symmetries of the moiré Hamiltonian H_+ can be represented by [73]

$$\hat{C}_{3z} = U_0(\mathbf{r}) \hat{R}_{3z} U_0^{\dagger}(\mathbf{r}), \quad \hat{C}_{2y} \hat{\mathcal{T}} = \sigma_x \hat{R}_{2y} \hat{\mathcal{T}}. \quad (\text{A10})$$

Under C_{3z} and $C_{2y}\mathcal{T}$ symmetries, the Hamiltonian of tMoTe₂ transforms as follows,

$$\begin{aligned}\hat{C}_{3z} H_+(\mathbf{k}, \mathbf{r}) \hat{C}_{3z}^{-1} &= H_+(\mathbf{k}, \mathbf{r}), \\ [\hat{C}_{2y} \hat{\mathcal{T}}] H_+(\mathbf{k}, \mathbf{r}) [\hat{C}_{2y} \hat{\mathcal{T}}]^{-1} &= H_+(\mathbf{k}, \mathbf{r}).\end{aligned}\quad (\text{A11})$$

Since $\Theta_{n,\mathbf{k}}^{(s)}(\mathbf{r})$ are basis functions to decompose Bloch states in tMoTe₂, we require that they are eigenstates of \hat{C}_{3z} at the threefold rotation invariant momentum

$\{\kappa_{\pm}, \gamma\}$, and also eigenstate of $\hat{C}_{2y}\hat{\mathcal{T}}$ at γ point. Constrained by these symmetries, $\Theta_{n,\mathbf{k}}^{(s)}(\mathbf{r})$ satisfies the following transformation rules:

$$\begin{aligned}\hat{C}_{3z}\Theta_{n,\mathbf{k}}^{(s)}(\mathbf{r}) &= e^{i\frac{2\pi}{3}L_{s,n,\mathbf{k}}}\Theta_{n,\mathbf{k}}^{(s)}(\mathbf{r}), \\ \hat{C}_{2y}\hat{\mathcal{T}}\Theta_{n,\gamma}^{(s)}(\mathbf{r}) &= e^{i\pi M_{s,n,\gamma}}\Theta_{n,\gamma}^{(s)}(\mathbf{r}),\end{aligned}\quad (\text{A12})$$

where $\mathbf{k} \in \{\kappa_{\pm}, \gamma\}$ are three high-symmetry points in mBZ for the first line. Here $L_{s,n,\mathbf{k}} \in \{-1, 0, 1\}$ and $M_{s,n,\gamma} \in \{0, 1\}$ are integers that label the eigenvalues of C_{3z} and $C_{2y}\hat{\mathcal{T}}$ symmetries, respectively. Therefore, $\mathcal{B}^{(s)}(\mathbf{r})$ must satisfy,

$$\hat{C}_{3z}\mathcal{B}^{(s)}(\mathbf{r}) = e^{iv_s}\mathcal{B}^{(s)}(\mathbf{r}), \quad (\text{A13})$$

$$\hat{C}_{2y}\hat{\mathcal{T}}\mathcal{B}^{(s)}(\mathbf{r}) = e^{iw_s}\mathcal{B}^{(s)}(\mathbf{r}), \quad (\text{A14})$$

where v_+ and w_+ are determined by the ansatz for $\mathcal{B}^{(+)}(\mathbf{r})$ given in Eq. (18).

We now demonstrate that $\mathcal{B}^{(-)}(\mathbf{r})$ in Eq. (19) satisfies Eqs. (A13) and (A14). For Eq. (A13), we have

$$\begin{aligned}\hat{C}_{3z}\mathcal{B}^{(-)}(\mathbf{r}) &= U_0(\mathbf{r})i\sigma_y[U_0^\dagger(\hat{R}_{3z}\mathbf{r})\mathcal{B}^{(+)}(\hat{R}_{3z}\mathbf{r})]^* \\ &= U_0(\mathbf{r})i\sigma_y[U_0^\dagger(\mathbf{r})\hat{C}_{3z}\mathcal{B}^{(+)}(\mathbf{r})]^* \\ &= e^{-iv_+}U_0(\mathbf{r})i\sigma_y[U_0^\dagger(\mathbf{r})\mathcal{B}^{(+)}(\mathbf{r})]^* \\ &= e^{-iv_+}\mathcal{B}^{(-)}(\mathbf{r}).\end{aligned}\quad (\text{A15})$$

Hence, Eq. (A13) is satisfied and $v_- = -v_+$. For Eq. (A14), we have

$$\begin{aligned}\hat{C}_{2y}\hat{\mathcal{T}}\mathcal{B}^{(-)}(\mathbf{r}) &= -e^{-i(\kappa_++\kappa_-)\cdot\hat{R}_{2y}\mathbf{r}}i\sigma_y\sigma_x[\mathcal{B}^{(+)}(\hat{R}_{2y}\mathbf{r})]^* \\ &= e^{-iw_++i\pi}\mathcal{B}^{(-)}(\mathbf{r}).\end{aligned}\quad (\text{A16})$$

Therefore Eq. (A14) is satisfied and we obtain $w_- = -w_+ + \pi$.

Appendix B: QGT of generalized LL

We now derive the QGT of the generalized LL wave function and prove the integrated form of the trace condition in Eq. (7). For simplicity, we focus on the orientation of magnetic field $s = -$, and the expressions for the $s = +$ case can be derived similarly. The QGT of the generalized LL wave function is determined by the Berry connection from equation

$$\begin{aligned}(\chi_{n,\mathbf{k}}^{(\text{gL})})_{ij} &= \langle \partial_{k_i}\tilde{\Theta}_{n,\mathbf{k}}^{(-)} | \partial_{k_j}\tilde{\Theta}_{n,\mathbf{k}}^{(-)} \rangle - \langle \partial_{k_i}\tilde{\Theta}_{n,\mathbf{k}}^{(-)} | \tilde{\Theta}_{n,\mathbf{k}}^{(-)} \rangle \langle \tilde{\Theta}_{n,\mathbf{k}}^{(-)} | \partial_{k_j}\tilde{\Theta}_{n,\mathbf{k}}^{(-)} \rangle \\ &= \sum_{m \neq n} A_{m,n,i}^* A_{m,n,j},\end{aligned}\quad (\text{B1})$$

where i, j are coordinate labels, and $\tilde{\Theta}_{n,\mathbf{k}}^{(-)}(\mathbf{r}) = e^{-i\mathbf{k}\cdot\mathbf{r}}\Theta_{n,\mathbf{k}}^{(-)}(\mathbf{r})$. The Berry connection $A_{m,n,j}$ is given by

$$A_{m,n,j} = i \langle \tilde{\Theta}_{m,\mathbf{k}}^{(-)} | \partial_{k_j} \tilde{\Theta}_{n,\mathbf{k}}^{(-)} \rangle. \quad (\text{B2})$$

The partial derivative operator ∂_{k_j} can be rewritten using the raising and lowering operators, b^\dagger and b , in momentum space

$$\begin{aligned}\partial_{k_x} &= \partial_{z_{\mathbf{k}}} + \partial_{z_{\mathbf{k}}^*} = \ell \frac{b - b^\dagger}{\sqrt{2}} - \frac{i\ell^2 k_y}{2}, \\ \partial_{k_y} &= i(\partial_{z_{\mathbf{k}}} - \partial_{z_{\mathbf{k}}^*}) = -i\ell \frac{b + b^\dagger}{\sqrt{2}} + \frac{i\ell^2 k_x}{2}.\end{aligned}\quad (\text{B3})$$

Here b and b^\dagger are obtained from a and a^\dagger by substituting $z \rightarrow i\ell^2 z_{\mathbf{k}}$,

$$b^\dagger = \frac{-2\ell^{-1}\partial_{z_{\mathbf{k}}} + \ell z_{\mathbf{k}}^*/2}{\sqrt{2}}, b = \frac{2\ell^{-1}\partial_{z_{\mathbf{k}}^*} + \ell z_{\mathbf{k}}/2}{\sqrt{2}}. \quad (\text{B4})$$

For the conventional LL wavefunction, we have the recurrence relation in the momentum space,

$$\tilde{\Psi}_{n,\mathbf{k}}^{(-)}(\mathbf{r}) = \frac{(b^\dagger)^n}{\sqrt{n!}} \tilde{\Psi}_{0,\mathbf{k}}^{(-)}(\mathbf{r}), \quad (\text{B5})$$

where $\tilde{\Psi}_{n,\mathbf{k}}^{(-)}(\mathbf{r}) = e^{-i\mathbf{k}\cdot\mathbf{r}}\Psi_{n,\mathbf{k}}^{(-)}(\mathbf{r})$.

We define the matrix element of b^\dagger and b operators in the generalized LL basis,

$$\gamma_{m,n,\mathbf{k}} = \langle \tilde{\Theta}_{m,\mathbf{k}}^{(-)} | b^\dagger \tilde{\Theta}_{n,\mathbf{k}}^{(-)} \rangle, \gamma'_{m,n,\mathbf{k}} = \langle \tilde{\Theta}_{m,\mathbf{k}}^{(-)} | b \tilde{\Theta}_{n,\mathbf{k}}^{(-)} \rangle, \quad (\text{B6})$$

which are related by $\gamma'_{m,n,\mathbf{k}} = \gamma_{n,m,\mathbf{k}}^*$. We note that the inner products used throughout this work are defined in real space, while the momentum index acts as a quantum number. The Berry connection can be expressed using these matrix elements as,

$$\begin{aligned}A_{m,n,x} &= i \frac{\ell}{\sqrt{2}} (\gamma_{n,m,\mathbf{k}}^* - \gamma_{m,n,\mathbf{k}}) + \frac{\ell^2}{2} k_y \delta_{m,n} \\ A_{m,n,y} &= \frac{\ell}{\sqrt{2}} (\gamma_{n,m,\mathbf{k}}^* + \gamma_{m,n,\mathbf{k}}) - \frac{\ell^2}{2} k_x \delta_{m,n}.\end{aligned}\quad (\text{B7})$$

We begin by proving that $\gamma_{m,n,\mathbf{k}}$ is nonzero only when $m = n$ and $m = n + 1$. For a linear combination of $\tilde{\Theta}_{m,\mathbf{k}}^{(-)}(\mathbf{r})$ denoted by $f(\mathbf{r})$, we have decomposition

$$f(\mathbf{r}) = \mathcal{B}^{(-)}(\mathbf{r})g(\mathbf{r}), \quad (\text{B8})$$

where $g(\mathbf{r})$ is a linear combination of $\tilde{\Psi}_{a,\mathbf{k}}^{(-)}(\mathbf{r})$ with a maximal LL index a_{max} . Specifically, $f(\mathbf{r}) = \tilde{\Theta}_{n,\mathbf{k}}^{(-)}(\mathbf{r})$ and $f(\mathbf{r}) = b^\dagger \tilde{\Theta}_{n,\mathbf{k}}^{(-)}(\mathbf{r})$ correspond to $a_{\text{max}} = n$ and $n + 1$, respectively. Therefore, $b^\dagger \tilde{\Theta}_{n,\mathbf{k}}^{(-)}(\mathbf{r})$ can be decomposed as,

$$b^\dagger \tilde{\Theta}_{n,\mathbf{k}}^{(-)}(\mathbf{r}) = \sum_{m=0}^{n+1} \gamma_{m,n,\mathbf{k}} \tilde{\Theta}_{m,\mathbf{k}}^{(-)}(\mathbf{r}), \quad (\text{B9})$$

which indicates that $\gamma_{m,n,\mathbf{k}} = 0$ for $m > n+1$. Similarly, we have

$$b\tilde{\Theta}_{n,\mathbf{k}}^{(-)}(\mathbf{r}) = \sum_{m=0}^n \gamma'_{m,n,\mathbf{k}} \tilde{\Theta}_{m,\mathbf{k}}^{(-)}(\mathbf{r}). \quad (\text{B10})$$

Therefore, $\gamma_{m,n,\mathbf{k}} = [\gamma'_{n,m,\mathbf{k}}]^* = 0$ for $m < n$.

We first determine $\gamma_{n+1,n,\mathbf{k}}$ through the following equation,

$$\begin{aligned} \gamma_{n+1,n,\mathbf{k}} &= \left\langle \tilde{\Theta}_{n+1,\mathbf{k}}^{(-)} \left| b^\dagger \mathcal{N}_{n,\mathbf{k}} \tilde{e}_{n,\mathbf{k}} \right. \right\rangle \\ &= \sqrt{n+1} \mathcal{N}_{n,\mathbf{k}} \left\langle \tilde{\Theta}_{n+1,\mathbf{k}}^{(-)} \left| \tilde{e}_{n+1,\mathbf{k}} \right. \right\rangle = \sqrt{n+1} \frac{\mathcal{N}_{n,\mathbf{k}}}{\mathcal{N}_{n+1,\mathbf{k}}}, \end{aligned} \quad (\text{B11})$$

where $\tilde{e}_{n,\mathbf{k}}(\mathbf{r}) = e^{-i\mathbf{k}\cdot\mathbf{r}} e_{n,\mathbf{k}}(\mathbf{r})$. We then obtain a recurrence relation for $\gamma_{n,n,\mathbf{k}}$ through the following relations,

$$\begin{aligned} &\left\langle b^\dagger \tilde{\Theta}_{n,\mathbf{k}}^{(-)} \left| b^\dagger \tilde{\Theta}_{n+1,\mathbf{k}}^{(-)} \right. \right\rangle \\ &= -\sqrt{2}\ell^{-1} \partial_{z_\mathbf{k}} \gamma_{n+1,n,\mathbf{k}} + \left\langle b\tilde{\Theta}_{n,\mathbf{k}}^{(-)} \left| b\tilde{\Theta}_{n+1,\mathbf{k}}^{(-)} \right. \right\rangle, \end{aligned} \quad (\text{B12})$$

$$\begin{aligned} &\left\langle b^\dagger \tilde{\Theta}_{n,\mathbf{k}}^{(-)} \left| b^\dagger \tilde{\Theta}_{n+1,\mathbf{k}}^{(-)} \right. \right\rangle \\ &= \left\langle b^\dagger \tilde{\Theta}_{n,\mathbf{k}}^{(-)} \left| \tilde{\Theta}_{n+1,\mathbf{k}}^{(-)} \right. \right\rangle \left\langle \tilde{\Theta}_{n+1,\mathbf{k}}^{(-)} \left| b^\dagger \tilde{\Theta}_{n+1,\mathbf{k}}^{(-)} \right. \right\rangle \\ &= \gamma_{n+1,n,\mathbf{k}} \gamma_{n+1,n+1,\mathbf{k}}, \end{aligned} \quad (\text{B13})$$

$$\begin{aligned} &\left\langle b\tilde{\Theta}_{n,\mathbf{k}}^{(-)} \left| b\tilde{\Theta}_{n+1,\mathbf{k}}^{(-)} \right. \right\rangle \\ &= \left\langle b\tilde{\Theta}_{n,\mathbf{k}}^{(-)} \left| \tilde{\Theta}_{n,\mathbf{k}}^{(-)} \right. \right\rangle \left\langle \tilde{\Theta}_{n,\mathbf{k}}^{(-)} \left| b\tilde{\Theta}_{n+1,\mathbf{k}}^{(-)} \right. \right\rangle \\ &= \gamma_{n+1,n,\mathbf{k}} \gamma_{n,n,\mathbf{k}}. \end{aligned} \quad (\text{B14})$$

The recurrence relation is

$$\gamma_{n+1,n+1,\mathbf{k}} = -\sqrt{2}\ell^{-1} \partial_{z_\mathbf{k}} \ln \gamma_{n+1,n,\mathbf{k}} + \gamma_{n,n,\mathbf{k}}. \quad (\text{B15})$$

Combining Eq. (B11) with the recurrence relation in Eq. (B15), we obtain the expression for $\gamma_{n,n,\mathbf{k}}$

$$\gamma_{n,n,\mathbf{k}} = \sqrt{2}\ell^{-1} \partial_{z_\mathbf{k}} \ln \mathcal{N}_{n,\mathbf{k}}. \quad (\text{B16})$$

The Berry connection has the following form,

$$A_{m,n,x} = \begin{cases} -\frac{i}{\sqrt{2}} \ell \gamma_{n+1,n,\mathbf{k}} & m = n+1 \\ -\partial_{k_x} \ln \mathcal{N}_{n,\mathbf{k}} + \frac{\ell^2 k_y}{2} & m = n \\ \frac{i}{\sqrt{2}} \ell \gamma_{n,n-1,\mathbf{k}} & m = n-1 \\ 0 & m \neq n+1, n, n-1 \end{cases}, \quad (\text{B17})$$

and

$$A_{m,n,y} = \begin{cases} \frac{1}{\sqrt{2}} \ell \gamma_{n+1,n,\mathbf{k}} & m = n+1 \\ \partial_{k_x} \ln \mathcal{N}_{n,\mathbf{k}} - \frac{\ell^2 k_x}{2} & m = n \\ \frac{1}{\sqrt{2}} \ell \gamma_{n,n-1,\mathbf{k}} & m = n-1 \\ 0 & m \neq n+1, n, n-1 \end{cases}. \quad (\text{B18})$$

After substituting Eqs. (B17) and (B18) into Eq. (B1), we derive the QGT for the generalized LL wave functions.

For $n = 0$, $\chi_{0,\mathbf{k}}^{(\text{gLL})}$ is given by

$$\chi_{0,\mathbf{k}}^{(\text{gLL})} = \gamma_{1,0,\mathbf{k}}^2 \ell^2 \left(-\frac{\frac{1}{2}}{\frac{i}{2}} \frac{\frac{i}{2}}{\frac{1}{2}} \right), \quad (\text{B19})$$

which clearly satisfies the trace condition $\text{Tr}[g_\mathbf{k}] = |\Omega_\mathbf{k}|$.

For $n \geq 1$, $\chi_{n,\mathbf{k}}^{(\text{gLL})}$ is formulated as

$$\chi_{n,\mathbf{k}}^{(\text{gLL})} = \ell^2 \left(\frac{\frac{1}{2}[\gamma_{n+1,n,\mathbf{k}}^2 + \gamma_{n,n-1,\mathbf{k}}^2]}{\frac{1}{2}[\gamma_{n+1,n,\mathbf{k}}^2 - \gamma_{n,n-1,\mathbf{k}}^2]} \frac{\frac{i}{2}[\gamma_{n+1,n,\mathbf{k}}^2 - \gamma_{n,n-1,\mathbf{k}}^2]}{\frac{1}{2}[\gamma_{n+1,n,\mathbf{k}}^2 + \gamma_{n,n-1,\mathbf{k}}^2]} \right). \quad (\text{B20})$$

We note that the Berry curvature can also be formulated as,

$$\Omega_{n,\mathbf{k}} = -2\text{Im}[\chi_{n,\mathbf{k}}^{(\text{gLL})}] = \partial_{k_x} A_{n,n,y} - \partial_{k_y} A_{n,n,x}, \quad (\text{B21})$$

from which we derive the recurrence relation for $\gamma_{n+1,n,\mathbf{k}}$

$$\gamma_{n+1,n,\mathbf{k}}^2 - \gamma_{n,n-1,\mathbf{k}}^2 = -4\ell^{-2} \partial_{z_\mathbf{k}} \partial_{z_\mathbf{k}}^* \ln \mathcal{N}_{n,\mathbf{k}} + 1. \quad (\text{B22})$$

Combining Eqs. (B11) and (B22), we obtain the recurrence relation for $\mathcal{N}_{n,\mathbf{k}}$

$$(n+1) \frac{\mathcal{N}_{n,\mathbf{k}}^2}{\mathcal{N}_{n+1,\mathbf{k}}^2} - n \frac{\mathcal{N}_{n-1,\mathbf{k}}^2}{\mathcal{N}_{n,\mathbf{k}}^2} = -4\ell^{-2} \partial_{z_\mathbf{k}} \partial_{z_\mathbf{k}}^* \ln \mathcal{N}_{n,\mathbf{k}} + 1. \quad (\text{B23})$$

This equation also applies to $n = 0$ with the understanding that $\mathcal{N}_{-1,\mathbf{k}} = 0$. Since $\mathcal{N}_{n,\mathbf{k}}$ is a continuous periodic function of \mathbf{k} , we establish the following formula

$$\frac{1}{2\pi} \int d^2\mathbf{k} \gamma_{n+1,n,\mathbf{k}}^2 = \ell^{-2} + \frac{1}{2\pi} \int d^2\mathbf{k} \gamma_{n,n-1,\mathbf{k}}^2. \quad (\text{B24})$$

Combining Eqs. (B20) and (B24), we obtain the integrated form of the trace condition in Eq. (7).

Appendix C: self-consistent HF method

We present a detailed description of the self-consistent HF method. The full many-body Hamiltonian of in tMoTe₂ in the hole basis is given by

$$\hat{H}^{(\text{full})} = \hat{H}_1 + \hat{H}_2 \quad (\text{C1})$$

The single-particle Hamiltonian \hat{H}_1 is

$$\hat{H}_1 = \sum_{\tau,n,\mathbf{k}} (-\mathcal{E}_{\tau,n,\mathbf{k}}) \varphi_{\tau,n,\mathbf{k}}^\dagger \varphi_{\tau,n,\mathbf{k}}, \quad (\text{C2})$$

where $-\mathcal{E}_{\tau,n,\mathbf{k}}$ is the single-particle energy in the hole basis. The interaction term \hat{H}_2 is

$$\begin{aligned} \hat{H}_2 &= \sum_{\tau,\tau'} \sum_{n_1,n_2,n_3,n_4} \sum_{\mathbf{k}_1,\mathbf{k}_2,\mathbf{k}_3,\mathbf{k}_4} V_{\mathbf{k}_1\mathbf{k}_2\mathbf{k}_3\mathbf{k}_4}^{\tau\tau' n_1 n_2 n_3 n_4} \\ &\quad \times \varphi_{\tau,n_1,\mathbf{k}_1}^\dagger \varphi_{\tau',n_2,\mathbf{k}_2}^\dagger \varphi_{\tau',n_3,\mathbf{k}_3} \varphi_{\tau,n_4,\mathbf{k}_4}. \end{aligned} \quad (\text{C3})$$

The interaction matrix element $V_{\mathbf{k}_1\mathbf{k}_2\mathbf{k}_3\mathbf{k}_4}^{\tau\tau' n_1 n_2 n_3 n_4}$ is given by

$$V_{\mathbf{k}_1\mathbf{k}_2\mathbf{k}_3\mathbf{k}_4}^{\tau\tau' n_1 n_2 n_3 n_4} = \frac{1}{2\mathcal{A}} \sum_{\mathbf{q}} V(\mathbf{q}) M_{\mathbf{k}_1\mathbf{k}_4}^{\tau n_1 n_4}(\mathbf{q}) M_{\mathbf{k}_2\mathbf{k}_3}^{\tau' n_2 n_3}(-\mathbf{q}), \quad (\text{C4})$$

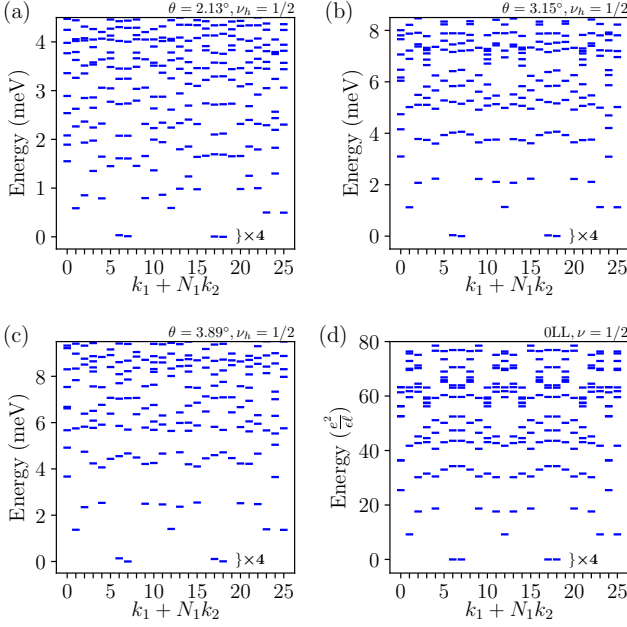


FIG. 14. (a-c) ED spectra of the original tMoTe₂ model at $\nu_h = 1/2$, where the twist angles are $\theta = 2.13^\circ, 3.15^\circ$, and 3.89° . (d) ED spectrum of the zeroth LL at $\nu = 1/2$. The energy scale is $e^2/(\epsilon\ell)$ with ℓ being the magnetic length. A 26 momentum cluster is employed.

where M is the plane-wave matrix element.

We then present the self-consistent HF method in the plane-wave basis. The hole creation (annihilation) operator in the plane-wave basis, $b_{\tau,\mathbf{k}+\mathbf{g},l}^\dagger$ ($b_{\tau,\mathbf{k}+\mathbf{g},l}$), are defined from

$$\begin{aligned} \varphi_{\tau,n,\mathbf{k}}^\dagger &= \sum_{\mathbf{g},l} U_{\tau,n,\mathbf{k}+\mathbf{g},l}^* b_{\tau,\mathbf{k}+\mathbf{g},l}^\dagger \\ \varphi_{\tau,n,\mathbf{k}} &= \sum_{\mathbf{g},l} U_{\tau,n,\mathbf{k}+\mathbf{g},l} b_{\tau,\mathbf{k}+\mathbf{g},l} \end{aligned} \quad (C5)$$

where \mathbf{g} represents the basis vector in mBZ and $U_{\tau,n,\mathbf{k}+\mathbf{g},l}$ satisfies

$$[h_{\tau,\mathbf{k}}]_{\mathbf{g}l,\mathbf{g}'l'} = \sum_n U_{\tau,n,\mathbf{k}+\mathbf{g},l} \mathcal{E}_{\tau,n,\mathbf{k}} U_{\tau,n,\mathbf{k}+\mathbf{g}',l'}^* \quad (C6)$$

where h_τ is the Hamiltonian of tMoTe₂ in the plane-wave basis. \hat{H}_1 and \hat{H}_2 are rewritten as

$$\begin{aligned} \hat{H}_1 &= - \sum_{\mathbf{k},\mathbf{g},\mathbf{g}'} \sum_{l,l'} \sum_{\tau} [h_{\tau,\mathbf{k}}^\dagger]_{\mathbf{g}l,\mathbf{g}'l'} b_{\tau,\mathbf{k}+\mathbf{g},l}^\dagger b_{\tau,\mathbf{k}+\mathbf{g}',l'} \\ \hat{H}_2 &= \frac{1}{2\mathcal{A}} \sum_{\mathbf{k},\mathbf{k}',\mathbf{q},\mathbf{g},\mathbf{g}'} \sum_{l,l',\tau,\tau'} V(\mathbf{q}) \\ &\quad \times b_{\tau,\mathbf{k}+\mathbf{g}+\mathbf{q},l}^\dagger b_{\tau',\mathbf{k}'+\mathbf{g}'-\mathbf{q},l'}^\dagger b_{\tau',\mathbf{k}'+\mathbf{g}',l'} b_{\tau,\mathbf{k}+\mathbf{g},l}. \end{aligned} \quad (C7)$$

Applying the HF approximation to $\hat{H}^{(\text{full})}$, we obtain

the mean-field Hamiltonian,

$$\begin{aligned} \hat{H}^{(\text{HF})} &= \\ &\sum_{\mathbf{k},\mathbf{g},\mathbf{g}'} \sum_{l,l'} \sum_{\tau} [-h_{\tau,\mathbf{k}}^\dagger + V_{\tau,\mathbf{k}}^{(\text{HF})}]_{\mathbf{g}l,\mathbf{g}'l'} b_{\tau,\mathbf{k}+\mathbf{g},l}^\dagger b_{\tau,\mathbf{k}+\mathbf{g}',l'} + E_0 \end{aligned} \quad (C8)$$

where $V_{\tau,\mathbf{k}}^{(\text{HF})}$ is the HF correction term given by

$$\begin{aligned} [V_{\tau,\mathbf{k}}^{(\text{HF})}]_{\mathbf{g}l,\mathbf{g}'l'} &= \delta_{ll'} \frac{1}{\mathcal{A}} \sum_{\mathbf{k}',\mathbf{g}''} \sum_{l'',\tau'} V(\mathbf{g} - \mathbf{g}') [n_{\tau',\mathbf{k}'}]_{(\mathbf{g}'+\mathbf{g}'')l'',(\mathbf{g}+\mathbf{g}'')l''} \\ &\quad - \frac{1}{\mathcal{A}} \sum_{\mathbf{k}',\mathbf{g}'} V(\mathbf{k}' - \mathbf{k} + \mathbf{g}'') [n_{\tau,\mathbf{k}'}]_{(\mathbf{g}'+\mathbf{g}'')l',(\mathbf{g}+\mathbf{g}'')l}. \end{aligned} \quad (C9)$$

and the constant energy term E_0 is

$$E_0 = -\frac{1}{2} \sum_{\mathbf{k},\mathbf{g},\mathbf{g}'} \sum_{l,l'} \sum_{\tau} [V_{\tau,\mathbf{k}}^{(\text{HF})}]_{\mathbf{g}l,\mathbf{g}'l'} [n_{\tau,\mathbf{k}}]_{\mathbf{g}l,\mathbf{g}'l'}. \quad (C10)$$

$n_{\tau,\mathbf{k}}$ is the density matrix

$$[n_{\tau,\mathbf{k}}]_{\mathbf{g}l,\mathbf{g}'l'} = \langle \Omega | b_{\mathbf{k}+\mathbf{g},l,\tau}^\dagger b_{\mathbf{k}+\mathbf{g}',l',\tau} | \Omega \rangle. \quad (C11)$$

Here $|\Omega\rangle$ denotes the ground state with the first band fully occupied when the filling factor $\nu_h = 2$ is considered,

$$|\Omega\rangle = \prod_{\tau=\pm} \prod_{i=1}^N \varphi_{\tau,1,\mathbf{k}_i}^\dagger |0\rangle \quad (C12)$$

$$= \prod_{\tau=\pm} \prod_{i=1}^N \sum_{\mathbf{g},l} U_{\tau,1,\mathbf{k}_i+\mathbf{g},l}^* b_{\tau,\mathbf{k}_i+\mathbf{g},l}^\dagger |0\rangle, \quad (C13)$$

Using a plane-wave cutoff of $|\mathbf{g}| \leq 5|\mathbf{g}_1|$, we carry out the self-consistent Hartree-Fock calculation iteratively. In each step, we diagonalize $\hat{H}^{(\text{HF})}$ and update $|\Omega\rangle$ with the resulting eigenstates, repeating until convergence is reached. This minimizes the total energy $E^{(\text{HF})}$ of the filled first band, which is expressed as

$$E^{(\text{HF})} = \langle \Omega | \hat{H}^{(\text{HF})} | \Omega \rangle \quad (C14)$$

$$= \sum_{\mathbf{k},\mathbf{g},\mathbf{g}'} \sum_{l,l'} \sum_{\tau} [-h_{\tau,\mathbf{k}}^\dagger + \frac{1}{2} V_{\tau,\mathbf{k}}^{(\text{HF})}]_{\mathbf{g}l,\mathbf{g}'l'} [n_{\tau,\mathbf{k}}]_{\mathbf{g}l,\mathbf{g}'l'}, \quad (C15)$$

and the convergence is reached when the change in the Hartree-Fock energy between successive iterations falls below 10^{-5} meV.

Appendix D: ED Calculation at $\nu_h=1/2$

Numerical results at $\nu_h = 1/2$ in tMoTe₂ are presented in Fig. 14(a-c) for a 26 momentum cluster. The energy spectra at $\theta = 2.13^\circ, 3.15^\circ$, and 3.89° exhibit a four-fold quasi-degenerate ground-state manifold. These four

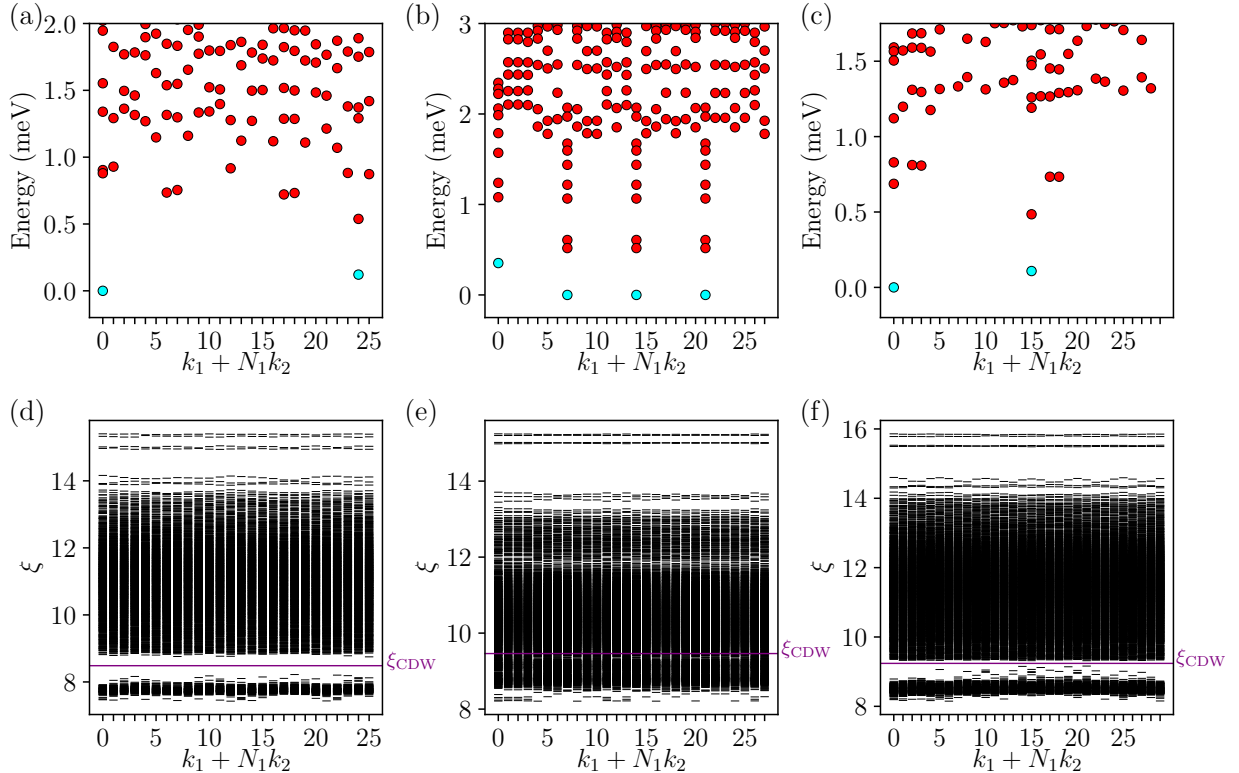


FIG. 15. (a-c) ED spectrum obtained at $\nu_h = 5/2$ and $\theta = 2.13^\circ$, using $N = 26, 28$, and 30 clusters. The quasi-degenerate states are highlighted in cyan. (d-f) PES with $N_A = 4$, for the quasi-degenerate states highlighted in cyan in (a-c).

quasi-degenerate states occur at momentum indices 6, 7, 17, and 18, which match with the momentum structure of a composite Fermi liquid in the zeroth LL at $\nu = 1/2$, as shown in Fig. 14(d). Across all twist angles studied from 2.13° to 3.89° , the 26-momentum cluster spectra provide robust evidence for a composite Fermi liquid at $\nu_h = 1/2$ in tMoTe₂. Furthermore, ED on clusters with even numbers of momentum points N from 16 to 30 at $\theta = 3.15^\circ$ consistently supports the presence of a composite Fermi liquid, demonstrating the stability of this phase across system sizes.

Appendix E: ED Calculation at $\theta = 2.13^\circ$

We present the numerical results at $\theta = 2.13^\circ$ and $\nu_h = 5/2$. The ED spectra and PES for clusters $N = 26, 28$, and 30 are shown in Fig. 15. Here we take $\lambda_w = 1$ and the wave function $\tilde{f}_{+,2,\mathbf{k}}(\mathbf{r}) = [\tilde{\psi}_{+,2,\mathbf{k}}(\mathbf{r})]^*$ in the projected Hamiltonian $\hat{\mathcal{H}}_2$. For the $N = 26$ cluster, a twofold quasi-degenerate ground states are located at momentum indices 0 and 24, which appears to be consistent with the MR momentum pattern. However, the PES reveals a different nature: instead of the entanglement gap associated with the MR state, it exhibits a clear gap at ξ_{CDW} and a low-lying level counting of $2\binom{13}{N_A}$, characteristic of

a CDW state. A similar situation occurs in the $N = 30$ cluster, where a twofold quasi-degeneracy is found at momentum indices 0 and 15, while the PES again shows a CDW-like entanglement gap with counting $2\binom{15}{N_A}$. For the $N = 28$ cluster, the sixfold MR degeneracy expected at momentum indices 7, 14, and 21 is lifted, and the low-energy states are redistributed across four momentum sectors at 0, 7, 14, and 21, corresponding to the mBZ center and the midpoints of the mBZ edges. This new momentum pattern is consistent with the CDW state. However, the PES does not show an entanglement gap at ξ_{CDW} , with a low-lying level counting of $4\binom{14}{N_A}$ expected for the CDW state, suggesting that the CDW phase is not yet fully developed.

We construct a phase diagram in the (λ_F, λ_w) parameter space for the three clusters, as shown in Fig. 16. Here, $\lambda_F \in [0, 1]$ controls the weight of the generalized 1LL in the wave function, as defined in Eq. (36), and $\lambda_w \in [0, 1]$ governs the bandwidth, as introduced in Eq. (28). At $\lambda_F = \lambda_w = 0$, the Hamiltonian corresponds to $\hat{\mathcal{H}}_{1gLL}$ defined in Sec. VI, where the wave function is the generalized 1LL obtained via variational mapping, and the bandwidth is set to zero. In this limit, MR states are observed, as characterized by both the ED spectra and the PES for all three clusters. The physical limit occurs at $\lambda_F = \lambda_w = 1$, where the ED spectra and PES presented in Fig. 15 indicate CDW state.

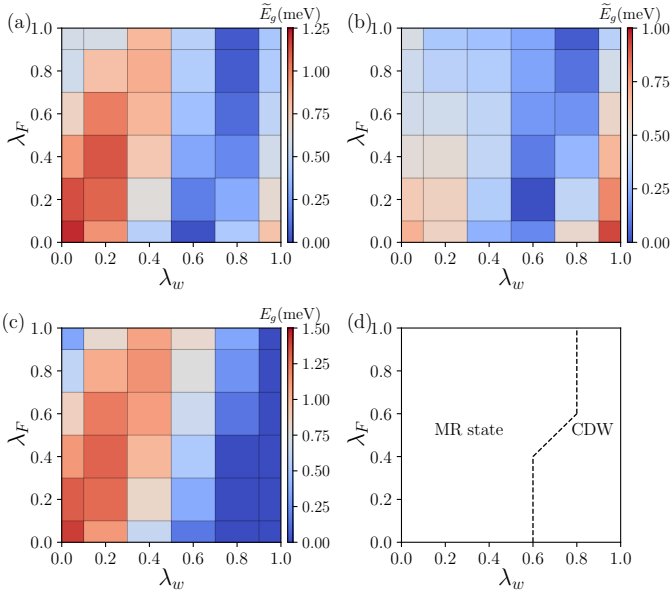


FIG. 16. Maps of the energy gap for quasi-degenerate states in the (λ_F, λ_w) parameter space for $\theta = 2.13^\circ$. (a) Direct gap \tilde{E}_g at the momentum index 24 sector in the $N = 26$ cluster. (b) Direct gap \tilde{E}_g at the momentum index 15 sector in the $N = 30$ cluster. (c) Gap E_g in the $N = 28$ cluster. (d) Schematic phase diagram. The dashed line, which connects the minima of \tilde{E}_g in the $N = 30$ cluster at fixed λ_F , provides an approximation to the phase boundary between the MR and CDW states.

For the system sizes $N = 26$ and $N = 30$, the direct gap at momentum index 0 remains finite throughout the (λ_F, λ_w) parameter space. We therefore use the direct gap \tilde{E}_g in momentum sectors 24 (15) for the $N = 26$ ($N = 30$) cluster to track the phase evolution. For $N = 28$ cluster, we use $E_g = E_7 - E_6$ where E_i is the i -th lowest energy level. Along the $\lambda_F = 0$ line, \tilde{E}_g decreases with increasing λ_w , reaches a minimum, and then rises again for both $N = 26$ and $N = 30$ clusters. Similarly, E_g decreases and finally vanishes as λ_w increases in the $N = 28$ cluster. These behaviors reflect transition between the MR and CDW states: increasing bandwidth destabilizes the MR phase and eventually favors the CDW state. As λ_F increases, this trend continues, with the transition point shifting toward larger values of λ_w . Notably, when the wave function slightly deviates from the generalized 1LL limit ($\lambda_F > 0$), the MR state becomes more robust against finite bandwidth. In the physical limit at $(\lambda_F, \lambda_w) = (1, 1)$, the system resides on the CDW side of the transition but can be driven into the MR phase by slightly reducing the bandwidth.

[1] D. C. Tsui, H. L. Stormer, and A. C. Gossard, Two-dimensional magnetotransport in the extreme quantum limit, *Phys. Rev. Lett.* **48**, 1559 (1982).

[2] R. B. Laughlin, Anomalous quantum Hall effect: An incompressible quantum fluid with fractionally charged excitations, *Phys. Rev. Lett.* **50**, 1395 (1983).

[3] F. D. M. Haldane, Fractional quantization of the Hall effect: A hierarchy of incompressible quantum fluid states, *Phys. Rev. Lett.* **51**, 605 (1983).

[4] B. I. Halperin, Statistics of quasiparticles and the hierarchy of fractional quantized Hall states, *Phys. Rev. Lett.* **52**, 1583 (1984).

[5] J. K. Jain, Composite-fermion approach for the fractional quantum Hall effect, *Phys. Rev. Lett.* **63**, 199 (1989).

[6] J. K. Jain, Theory of the fractional quantum Hall effect, *Phys. Rev. B* **41**, 7653 (1990).

[7] R. Willett, J. P. Eisenstein, H. L. Störmer, D. C. Tsui, A. C. Gossard, and J. H. English, Observation of an even-denominator quantum number in the fractional quantum Hall effect, *Phys. Rev. Lett.* **59**, 1776 (1987).

[8] G. Moore and N. Read, Nonabelions in the fractional quantum Hall effect, *Nuclear Physics B* **360**, 362 (1991).

[9] N. Read and G. Moore, Fractional quantum Hall effect and nonabelian statistics, *Progress of Theoretical Physics Supplement* **107**, 157 (1992).

[10] N. Read and D. Green, Paired states of fermions in two dimensions with breaking of parity and time-reversal symmetries and the fractional quantum Hall effect, *Phys. Rev. B* **61**, 10267 (2000).

[11] S. Das Sarma, M. Freedman, and C. Nayak, Topologically protected qubits from a possible non-abelian fractional quantum Hall state, *Phys. Rev. Lett.* **94**, 166802 (2005).

[12] E. Tang, J.-W. Mei, and X.-G. Wen, High-temperature fractional quantum Hall states, *Phys. Rev. Lett.* **106**, 236802 (2011).

[13] K. Sun, Z. Gu, H. Katsura, and S. Das Sarma, Nearly flatbands with nontrivial topology, *Phys. Rev. Lett.* **106**, 236803 (2011).

[14] T. Neupert, L. Santos, C. Chamon, and C. Mudry, Fractional quantum Hall states at zero magnetic field, *Phys. Rev. Lett.* **106**, 236804 (2011).

[15] N. Regnault and B. A. Bernevig, Fractional Chern insulator, *Phys. Rev. X* **1**, 021014 (2011).

[16] D. N. Sheng, Z.-C. Gu, K. Sun, and L. Sheng, Fractional quantum Hall effect in the absence of Landau levels, *Nature Communications* **2**, 389 (2011).

[17] J. Cai, E. Anderson, C. Wang, X. Zhang, X. Liu, W. Holtzmann, Y. Zhang, F. Fan, T. Taniguchi, K. Watanabe, Y. Ran, T. Cao, L. Fu, D. Xiao, W. Yao, and X. Xu, Signatures of fractional quantum anomalous Hall states in twisted MoTe₂, *Nature* **622**, 63 (2023).

[18] Y. Zeng, Z. Xia, K. Kang, J. Zhu, P. Knüppel, C. Vaswani, K. Watanabe, T. Taniguchi, K. F. Mak, and J. Shan, Thermodynamic evidence of fractional Chern

insulator in moiré MoTe₂, *Nature* **622**, 69 (2023).

[19] H. Park, J. Cai, E. Anderson, Y. Zhang, J. Zhu, X. Liu, C. Wang, W. Holtzmann, C. Hu, Z. Liu, T. Taniguchi, K. Watanabe, J.-H. Chu, T. Cao, L. Fu, W. Yao, C.-Z. Chang, D. Cobden, D. Xiao, and X. Xu, Observation of fractionally quantized anomalous Hall effect, *Nature* **622**, 74 (2023).

[20] F. Xu, Z. Sun, T. Jia, C. Liu, C. Xu, C. Li, Y. Gu, K. Watanabe, T. Taniguchi, B. Tong, J. Jia, Z. Shi, S. Jiang, Y. Zhang, X. Liu, and T. Li, Observation of integer and fractional quantum anomalous Hall effects in twisted bilayer MoTe₂, *Phys. Rev. X* **13**, 031037 (2023).

[21] Z. Lu, T. Han, Y. Yao, A. P. Reddy, J. Yang, J. Seo, K. Watanabe, T. Taniguchi, L. Fu, and L. Ju, Fractional quantum anomalous Hall effect in multilayer graphene, *Nature* **626**, 759 (2024).

[22] J. Xie, Z. Huo, X. Lu, Z. Feng, Z. Zhang, W. Wang, Q. Yang, K. Watanabe, T. Taniguchi, K. Liu, Z. Song, X. C. Xie, J. Liu, and X. Lu, Tunable fractional Chern insulators in rhombohedral graphene superlattices, *Nature Materials* **24**, 1042 (2025).

[23] A. P. Reddy and L. Fu, Toward a global phase diagram of the fractional quantum anomalous Hall effect, *Phys. Rev. B* **108**, 245159 (2023).

[24] A. P. Reddy, F. Alsallom, Y. Zhang, T. Devakul, and L. Fu, Fractional quantum anomalous Hall states in twisted bilayer MoTe₂ and WSe₂, *Phys. Rev. B* **108**, 085117 (2023).

[25] C. Wang, X.-W. Zhang, X. Liu, Y. He, X. Xu, Y. Ran, T. Cao, and D. Xiao, Fractional Chern insulator in twisted bilayer MoTe₂, *Phys. Rev. Lett.* **132**, 036501 (2024).

[26] C. Xu, J. Li, Y. Xu, Z. Bi, and Y. Zhang, Maximally localized Wannier functions, interaction models, and fractional quantum anomalous Hall effect in twisted bilayer MoTe₂, *Proceedings of the National Academy of Sciences* **121**, e2316749121 (2024).

[27] N. Mao, C. Xu, J. Li, T. Bao, P. Liu, Y. Xu, C. Felser, L. Fu, and Y. Zhang, Transfer learning relaxation, electronic structure and continuum model for twisted bilayer MoTe₂, *Communications Physics* **7**, 262 (2024).

[28] J. Yu, J. Herzog-Arbeitman, M. Wang, O. Vafek, B. A. Bernevig, and N. Regnault, Fractional Chern insulators versus nonmagnetic states in twisted bilayer MoTe₂, *Phys. Rev. B* **109**, 045147 (2024).

[29] A. Abouelkomsan, A. P. Reddy, L. Fu, and E. J. Bergholtz, Band mixing in the quantum anomalous Hall regime of twisted semiconductor bilayers, *Phys. Rev. B* **109**, L121107 (2024).

[30] X.-Y. Song, Y.-H. Zhang, and T. Senthil, Phase transitions out of quantum Hall states in moiré materials, *Phys. Rev. B* **109**, 085143 (2024).

[31] N. Morales-Durán, N. Wei, J. Shi, and A. H. MacDonald, Magic angles and fractional Chern insulators in twisted homobilayer transition metal dichalcogenides, *Phys. Rev. Lett.* **132**, 096602 (2024).

[32] T. Lu and L. H. Santos, Fractional Chern insulators in twisted bilayer MoTe₂: A composite fermion perspective, *Phys. Rev. Lett.* **133**, 186602 (2024).

[33] Z. Liu, B. Li, Y. Shi, and F. Wu, Characterization of fractional Chern insulator quasiparticles in twisted homobilayer MoTe₂, *Phys. Rev. B* **112**, 245104 (2025).

[34] M. Gonçalves, J. F. Mendez-Valderrama, J. Herzog-Arbeitman, J. Yu, X. Xu, D. Xiao, B. A. Bernevig, and N. Regnault, Spinless and spinful charge excitations in moiré fractional Chern insulators, [arXiv:2506.05330](https://arxiv.org/abs/2506.05330).

[35] H. Goldman, A. P. Reddy, N. Paul, and L. Fu, Zero-field composite Fermi liquid in twisted semiconductor bilayers, *Phys. Rev. Lett.* **131**, 136501 (2023).

[36] J. Dong, J. Wang, P. J. Ledwith, A. Vishwanath, and D. E. Parker, Composite Fermi liquid at zero magnetic field in twisted MoTe₂, *Phys. Rev. Lett.* **131**, 136502 (2023).

[37] C.-M. Jian, M. Cheng, and C. Xu, Minimal fractional topological insulator in half-filled conjugate moiré Chern bands, *Phys. Rev. X* **15**, 021063 (2025).

[38] Y.-H. Zhang, Non-abelian and abelian descendants of a vortex spin liquid: Fractional quantum spin Hall effect in twisted MoTe₂, *Phys. Rev. B* **110**, 155102 (2024).

[39] C.-E. Ahn, W. Lee, K. Yananose, Y. Kim, and G. Y. Cho, Non-abelian fractional quantum anomalous Hall states and first Landau level physics of the second moiré band of twisted bilayer MoTe₂, *Phys. Rev. B* **110**, L161109 (2024).

[40] J. May-Mann, A. Stern, and T. Devakul, Theory of half-integer fractional quantum spin Hall edges, *Phys. Rev. B* **111**, L201111 (2025).

[41] C. Xu, N. Mao, T. Zeng, and Y. Zhang, Multiple Chern bands in twisted MoTe₂ and possible non-Abelian states, *Phys. Rev. Lett.* **134**, 066601 (2025).

[42] F. Chen, W.-W. Luo, W. Zhu, and D. N. Sheng, Robust non-Abelian even-denominator fractional Chern insulator in twisted bilayer MoTe₂, *Nature Communications* **16**, 2115 (2025).

[43] C. Wang, X.-W. Zhang, X. Liu, J. Wang, T. Cao, and D. Xiao, Higher Landau-level analogs and signatures of non-Abelian states in twisted bilayer MoTe₂, *Phys. Rev. Lett.* **134**, 076503 (2025).

[44] A. P. Reddy, N. Paul, A. Abouelkomsan, and L. Fu, Non-abelian fractionalization in topological minibands, *Phys. Rev. Lett.* **133**, 166503 (2024).

[45] X.-L. Qi, Generic wave-function description of fractional quantum anomalous Hall states and fractional topological insulators, *Phys. Rev. Lett.* **107**, 126803 (2011).

[46] Y.-L. Wu, N. Regnault, and B. A. Bernevig, Gauge-fixed Wannier wave functions for fractional topological insulators, *Phys. Rev. B* **86**, 085129 (2012).

[47] S. A. Parameswaran, R. Roy, and S. L. Sondhi, Fractional quantum Hall physics in topological flat bands, *Comptes Rendus. Physique* **14**, 816 (2013).

[48] T. S. Jackson, G. Möller, and R. Roy, Geometric stability of topological lattice phases, *Nature Communications* **6**, 8629 (2015).

[49] M. Claassen, C. H. Lee, R. Thomale, X.-L. Qi, and T. P. Devereaux, Position-momentum duality and fractional quantum Hall effect in Chern insulators, *Phys. Rev. Lett.* **114**, 236802 (2015).

[50] G. Tarnopolsky, A. J. Kruchkov, and A. Vishwanath, Origin of magic angles in twisted bilayer graphene, *Phys. Rev. Lett.* **122**, 106405 (2019).

[51] P. J. Ledwith, G. Tarnopolsky, E. Khalaf, and A. Vishwanath, Fractional Chern insulator states in twisted bilayer graphene: An analytical approach, *Phys. Rev. Res.* **2**, 023237 (2020).

[52] J. Wang, Y. Zheng, A. J. Millis, and J. Cano, Chiral approximation to twisted bilayer graphene: Exact intravalley inversion symmetry, nodal structure, and implications for higher magic angles, *Phys. Rev. Res.* **3**, 023155 (2021).

[53] J. Wang, J. Cano, A. J. Millis, Z. Liu, and B. Yang, Exact Landau level description of geometry and interaction in a flatband, *Phys. Rev. Lett.* **127**, 246403 (2021).

[54] T. Ozawa and B. Mera, Relations between topology and the quantum metric for Chern insulators, *Phys. Rev. B* **104**, 045103 (2021).

[55] B. Mera and T. Ozawa, Kähler geometry and Chern insulators: Relations between topology and the quantum metric, *Phys. Rev. B* **104**, 045104 (2021).

[56] J. Wang and Z. Liu, Hierarchy of ideal flatbands in chiral twisted multilayer graphene models, *Phys. Rev. Lett.* **128**, 176403 (2022).

[57] P. J. Ledwith, A. Vishwanath, and E. Khalaf, Family of ideal Chern flatbands with arbitrary Chern number in chiral twisted graphene multilayers, *Phys. Rev. Lett.* **128**, 176404 (2022).

[58] P. J. Ledwith, A. Vishwanath, and D. E. Parker, Vortexability: A unifying criterion for ideal fractional Chern insulators, *Phys. Rev. B* **108**, 205144 (2023).

[59] J. Wang, S. Klevtsov, and Z. Liu, Origin of model fractional Chern insulators in all topological ideal flatbands: Explicit color-entangled wave function and exact density algebra, *Phys. Rev. Res.* **5**, 023167 (2023).

[60] J. Dong, P. J. Ledwith, E. Khalaf, J. Y. Lee, and A. Vishwanath, Many-body ground states from decomposition of ideal higher Chern bands: Applications to chirally twisted graphene multilayers, *Phys. Rev. Res.* **5**, 023166 (2023).

[61] N. Morales-Durán, N. Wei, J. Shi, and A. H. MacDonald, Magic angles and fractional Chern insulators in twisted homobilayer transition metal dichalcogenides, *Phys. Rev. Lett.* **132**, 096602 (2024).

[62] J. Shi, N. Morales-Durán, E. Khalaf, and A. H. MacDonald, Adiabatic approximation and Aharonov-Casher bands in twisted homobilayer transition metal dichalcogenides, *Phys. Rev. B* **110**, 035130 (2024).

[63] B. Li and F. Wu, Variational mapping of Chern bands to Landau levels: Application to fractional Chern insulators in twisted MoTe₂, *Phys. Rev. B* **111**, 125122 (2025).

[64] M. Fujimoto, D. E. Parker, J. Dong, E. Khalaf, A. Vishwanath, and P. Ledwith, Higher vortexability: Zero-field realization of higher landau levels, *Phys. Rev. Lett.* **134**, 106502 (2025).

[65] Y. Aharonov and A. Casher, Ground state of a spin- $\frac{1}{2}$ charged particle in a two-dimensional magnetic field, *Phys. Rev. A* **19**, 2461 (1979).

[66] F. Wu, T. Lovorn, E. Tutuc, I. Martin, and A. H. MacDonald, Topological insulators in twisted transition metal dichalcogenide homobilayers, *Phys. Rev. Lett.* **122**, 086402 (2019).

[67] Z. Liu, B. Mera, M. Fujimoto, T. Ozawa, and J. Wang, Theory of generalized Landau levels and its implications for non-Abelian states, *Phys. Rev. X* **15**, 031019 (2025).

[68] Y. Zhang, H. Pi, J. Liu, W. Miao, Z. Qi, N. Regnault, H. Weng, X. Dai, B. A. Bernevig, Q. Wu, and J. Yu, Universal moiré-model-building method without fitting: Application to twisted MoTe₂ and WSe₂, [arXiv:2411.08108](https://arxiv.org/abs/2411.08108).

[69] F. Xu, X. Chang, J. Xiao, Y. Zhang, F. Liu, Z. Sun, N. Mao, N. Peshcherenko, J. Li, K. Watanabe, T. Taniguchi, B. Tong, L. Lu, J. Jia, D. Qian, Z. Shi, Y. Zhang, X. Liu, S. Jiang, and T. Li, Interplay between topology and correlations in the second moiré band of twisted bilayer MoTe₂, *Nature Physics* **21**, 542 (2025).

[70] H. Park, J. Cai, E. Anderson, X.-W. Zhang, X. Liu, W. Holtzmann, W. Li, C. Wang, C. Hu, Y. Zhao, T. Taniguchi, K. Watanabe, J. Yang, D. Cobden, J.-h. Chu, N. Regnault, B. A. Bernevig, L. Fu, T. Cao, D. Xiao, and X. Xu, Ferromagnetism and topology of the higher flat band in a fractional Chern insulator, *Nature Physics* **21**, 549 (2025).

[71] L. An, H. Pan, W.-X. Qiu, N. Wang, S. Ru, Q. Tan, X. Dai, X. Cai, Q. Shang, X. Lu, H. Jiang, X. Lyu, S. Yang, K. Watanabe, T. Taniguchi, F. Wu, and W.-b. Gao, Observation of ferromagnetic phase in the second moiré band of twisted MoTe₂, *Nature Communications* **16**, 5131 (2025).

[72] Y. Onishi and L. Fu, Quantum weight: A fundamental property of quantum many-body systems, *Phys. Rev. Res.* **7**, 023158 (2025).

[73] F. D. M. Haldane, A modular-invariant modified Weierstrass sigma-function as a building block for lowest-Landau-level wavefunctions on the torus, *Journal of Mathematical Physics* **59**, 071901 (2018).

[74] See <https://github.com/zhangyan31415/continuum-model-twist-tmds> for the model parameters.

[75] F. D. M. Haldane, “fractional statistics” in arbitrary dimensions: A generalization of the Pauli principle, *Phys. Rev. Lett.* **67**, 937 (1991).

[76] B. A. Bernevig and N. Regnault, Emergent many-body translational symmetries of Abelian and non-Abelian fractionally filled topological insulators, *Phys. Rev. B* **85**, 075128 (2012).

[77] H. Liu, Z. Liu, and E. J. Bergholtz, Non-abelian fractional Chern insulators and competing states in flat moiré bands, *Phys. Rev. Lett.* **135**, 106604 (2025).

[78] A. Sterdyniak, N. Regnault, and B. A. Bernevig, Extracting excitations from model state entanglement, *Phys. Rev. Lett.* **106**, 100405 (2011).

[79] N. Read, Wavefunctions and counting formulas for quasi-holes of clustered quantum Hall states on a sphere, *Phys. Rev. B* **73**, 245334 (2006).

[80] N. Read and E. Rezayi, Beyond paired quantum hall states: Parafermions and incompressible states in the first excited landau level, *Phys. Rev. B* **59**, 8084 (1999).

[81] C. Nayak, S. H. Simon, A. Stern, M. Freedman, and S. Das Sarma, Non-abelian anyons and topological quantum computation, *Rev. Mod. Phys.* **80**, 1083 (2008).

[82] E. H. Rezayi and N. Read, Non-abelian quantized Hall states of electrons at filling factors 12/5 and 13/5 in the first excited Landau level, *Phys. Rev. B* **79**, 075306 (2009).

[83] F. Xu, Z. Sun, J. Li, C. Zheng, C. Xu, J. Gao, T. Jia, K. Watanabe, T. Taniguchi, B. Tong, L. Lu, J. Jia, Z. Shi, S. Jiang, Y. Zhang, Y. Zhang, S. Lei, X. Liu, and T. Li, Signatures of unconventional superconductivity near reentrant and fractional quantum anomalous hall insulators, [arXiv:2504.06972](https://arxiv.org/abs/2504.06972).

[84] W. Li, C. Beach, C. Hu, J.-H. Chu, L. Fu, T. Cao, D. Xiao, and X. Xu, Quantum sensing abundant Jain sequence fractional Chern insulators, *APS March Meeting 2025*.

[85] H. Pan, S. Yang, Y. Wang, X. Cai, W. Wang, Y. Zhao, K. Watanabe, T. Taniguchi, L. Zhang, Y. Liu, B. Yang, and W. Gao, Optical signatures of -1/3 fractional quantum anomalous Hall state in twisted MoTe₂, *Phys. Rev. Lett.* , (2026).

[86] X. Li, Y. Chen, B. Li, H. Chen, F. Wu, J. Chen, and W. Ren, Deep learning sheds light on integer and frac-

tional topological insulators, [arXiv:2503.11756](https://arxiv.org/abs/2503.11756).

[87] W. Yang, D. Zhai, T. Tan, F.-R. Fan, Z. Lin, and W. Yao, Fractional quantum anomalous Hall effect in a singular flat band, *Phys. Rev. Lett.* **134**, 196501 (2025).

[88] H. Lu and W. Yao, Bosonic Laughlin and moore-read states from non-Chern flat bands, [arXiv:2510.14685](https://arxiv.org/abs/2510.14685).

[89] H. Liu, R. Perea-Causin, Z. Liu, and E. J. Bergholtz, Topological order without band topology in moiré graphene, [arXiv:2510.15027](https://arxiv.org/abs/2510.15027).

[90] Z. Lin, H. Lu, W. Yang, D. Zhai, and W. Yao, Fractional Chern insulator states in an isolated flat band of zero Chern number, *Newton* [10.1016/j.newton.2025.100339](https://doi.org/10.1016/j.newton.2025.100339) (2026).